Contents lists available at ScienceDirect

Geochimica et Cosmochimica Acta

journal homepage: www.elsevier.com/locate/gca

Pyrite trace element proxies for magmatic volatile influx in submarine subduction-related hydrothermal systems

Jan J. Falkenberg [a,*], Manuel Keith [a], Karsten M. Haase [a], Reiner Klemd [a], Martin Kutzschbach [b], Anna Grosche [a], Maria Rosa Scicchitano [c], Harald Strauss [d], Jonguk Kim [e]

[a] GeoZentrum Nordbayern, Friedrich-Alexander-Universität (FAU) Erlangen-Nürnberg, Schlossgarten 5, 91054 Erlangen, Germany
[b] Technische Universität Berlin, Chair of Applied Geochemistry, 10587 Berlin, Germany
[c] Deutsches GeoForschungsZentrum GFZ, 14473 Potsdam, Germany
[d] Institut für Geologie und Paläontologie, Universität Münster, Münster, Germany
[e] Ocean Georesources Research Department, Korean Institute of Ocean Science & Technology, 385 Haeyang-ro, Yeongdo-gu, Busan 49111, Republic of Korea

ARTICLE INFO

ABSTRACT

Seafloor massive sulfides are modern analogues to ancient volcanogenic massive sulfide deposits, which are particularly enriched in volatile and precious metals (e.g., Te, Au, Ag, Cu, Bi, Se) in subduction-related settings. However, the sources of metals are still poorly constrained, and it remains elusive, whether magmatic volatile influx controls their distribution in submarine hydrothermal systems on the plate tectonic-scale. Here, we demonstrate, for the first time, that Te, As, and Sb contents as well as related Te/As and Te/Sb ratios vary systematically with the δ^{34}S composition of pyrite and native S, as reported by high-resolution coupled SIMS δ^{34}S and trace element LA-ICP-MS micro-analysis. The better correlation of element ratios (Te/As, Te/Sb) opposed to trace element contents (e.g., Te) with δ^{34}S in pyrite demonstrates that element ratios provide a more robust record of magmatic volatile influx than their absolute contents. On this basis, we define a quantitative threshold of high Te/As (>0.004) and Te/Sb (>0.6) ratios in pyrite that are indicative of magmatic volatile influx to submarine subduction-related hydrothermal systems. Two-component fluid mixing simulations further revealed that <5 % of magmatic volatile influx drastically changes the Te/As (and Te/Sb) ratio of the modelled fluid, but only slightly changes its δ^{34}S composition. This suggests that Te/As and Te/Sb ratios are more sensitive to a magmatic volatile influx into seawater-dominated hydrothermal systems than δ^{34}S signatures if the magmatic volatile influx was low. Beyond this, our results demonstrate that magma-derived fluid mixing with seawater only has a negligible effect on the magmatic volatile record of Te/As and Te/Sb, while the S isotope system is prone for seawater overprinting leading to commonly ambiguous source signatures. Thus, Te/As and Te/Sb systematics in pyrite provide a robust proxy to evaluate the contribution of magmatic volatiles to submarine hydrothermal systems from the grain- to plate tectonic-scale.

1. Introduction

Hydrothermal fluid circulation in the oceanic crust drives the chemical exchange and heat transfer between the lithosphere and the oceans (Früh-Green et al., 2022; Hannington et al., 2005; Schwarzenbach and Steele-MacInnis, 2020). These processes result in the discharge of high-temperature (up to 464 °C) metal-bearing fluids from hydrothermal vents on the modern seafloor causing the formation of seafloor massive sulfides (SMS) that are preserved as volcanogenic massive sulfide (VMS) deposits in the geological record (Galley and Koski, 1999;

Hannington et al., 2005; Koschinsky et al., 2008; Petersen et al., 2018). At mid-ocean ridges, heated seawater-derived fluids leach the adjacent host rocks causing metal mobilization, which subsequently precipitate as hydrothermal sulfides upon mixing of the hot fluid and cold ambient seawater (Früh-Green et al., 2022; Hannington et al., 2005; Petersen et al., 2018). Similar processes occur at island arc volcanoes and in back-arc basins, but subduction-related SMS and VMS are known to be enriched in precious and volatile elements (e.g., Te, Se, Bi, Cu, Au, Ag) compared to their mid-ocean ridge counterparts (Galley and Koski, 1999; Hannington et al., 2005; Monecke et al., 2016). However, it

remains unclear whether the enrichment of these volatile and precious metals in subduction-related submarine hydrothermal systems is due to the interaction of the fluids with more felsic crustal rocks, linked to the influx of a metal-bearing magmatic volatile phase (MVP), and/or the result of distinct hydrothermal fractionation and precipitation processes compared to MOR settings (Hannington et al., 2005; Kim et al., 2011; Monecke et al., 2016; Toffolo et al., 2020; Yang and Scott, 2006).

Pyrite is by far the most common sulfide in various hydrothermal environments and is host to a wide range of trace elements (Börner et al., 2023; Deditius et al., 2011; Reich et al., 2005). Its trace element content and S isotope composition can record variable metal sources, physico-chemical fluid conditions (e.g., temperature, salinity, fO_2), and related hydrothermal processes, such as phase separation and fluid mixing (Falkenberg et al., 2021; Grosche et al., 2023; Martin et al., 2022a, 2022b; Paton et al., 2011; Román et al., 2019). The contribution of a MVP to a hydrothermal system is documented by S isotope fractionation induced by the disproportionation of magmatic SO_2. This results in low and mostly negative $\delta^{34}S$ values in the respective sulfide precipitates and the H_2S portion of the hydrothermal fluids relative to the $\delta^{34}S$ composition of the associated host rocks (Herzig et al., 1998; Kusakabe et al., 2000; McDermott et al., 2015). Furthermore, a MVP influx has been inferred to be recorded by "high" contents of volatile elements like Te, Se, Cu, and Bi, but quantitative thresholds based on trace element contents or ratios are yet to be constrained (de Ronde et al., 2011; Grosche et al., 2023; Keith et al., 2016; Martin et al., 2020, 2022b; Wohlgemuth-Ueberwasser et al., 2015). Negative $\delta^{34}S$ values in hydrothermal pyrite that are indicative of MVP influx were reported for subduction-related submarine environments, such as the active NW caldera vent site at Brothers volcano (-5.6 to 3.0 ‰; de Ronde et al., 2001, 2011) and Hine Hina at the Valu Fa Ridge (-7.7 ‰ to -2.4 ‰; Herzig et al., 1998), but also in ancient VMS deposits, such as those of the Troodos ophiolite, Cyprus (-5.5 to 13.2 ‰; Martin et al., 2020). However, it remains ambiguous, whether MVP influx recorded by low $\delta^{34}S$ signatures is genetically linked to the enrichment of volatile and precious metals (e.g., Au, Te, Cu, As, Sb, Se, and Bi) in subduction-related hydrothermal systems, since coupled trace element and S isotope data in hydrothermal sulfides are scarce. Here, we demonstrate, for the first time, using coupled SIMS $\delta^{34}S$ isotope and LA-ICP-MS trace element micro-analysis of hydrothermal pyrite (and native S) from various subduction-related vent sites, that the contribution of a MVP results in a covariation between S isotope signatures and related Te/As and Te/Sb ratios from the grain- to plate tectonic-scale.

2. Geological overview and sample localities

The studied SMS samples were collected during research cruises of R/V Sonne (SO135, SO192/2, SO216, SO229, SO263) and R/V Onnuri (H-06) in the Pacific Ocean (Fig. 1). This includes the Tonga-Kermadec arc with the arc front volcanoes Niua South (Falkenberg et al., 2021; Gartman et al., 2019), Brothers volcano (de Ronde et al., 2011), and Volcano 19 (Stoffers et al., 2006), as well as the Niuatahi volcano (Falkenberg et al., 2022; Kim et al., 2011) in the rear-arc. These volcanos are host to several hydrothermal active vent sites associated with younger magmatic cones (i.e., Brothers upper and lower cone, Volcano 19 cone, Niuatahi Southcentral, Niuatahi Southwest, and Niuatahi Motutahi), and hydrothermal venting in proximity to caldera ring fault structures (Brothers NW caldera, Volcano 19 caldera wall, Niuatahi North) (de Ronde et al., 2011; Falkenberg et al., 2022; Kim et al., 2011; Stoffers et al., 2006). Samples from back-arc hydrothermal systems were studied from Hine Hina at the Valu Fa Ridge (Herzig et al., 1998), Maka South at the NE Lau spreading center (Klose et al., 2021), Nifonea caldera in the New Hebrides basin (Keith et al., 2021; Schmidt et al., 2017), and Satanic Mills from the Eastern Manus basin (Reeves et al., 2011). The sample set (Table 1) was supplemented by previously published pyrite and native S data from these localities, as well as from the Okinawa Trough (Iheya North, Jade, Yonaguni Knoll; Choi et al., 2022;
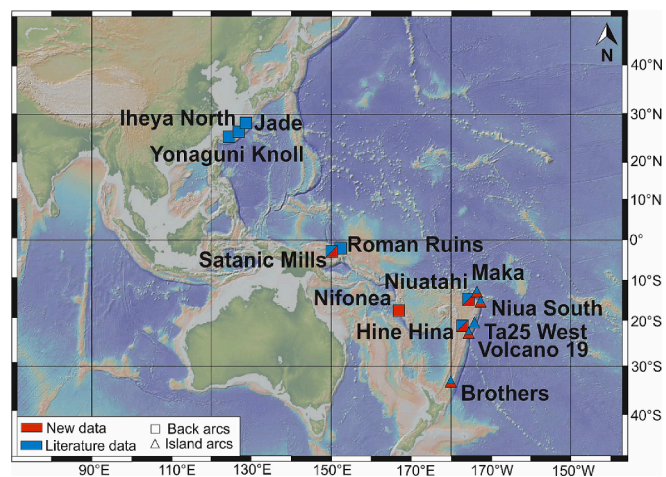

Fig. 1. Bathymetric map of the western Pacific Ocean (GEBCO Bathymetric Compilation Group, 2020), showing the locations of the island arc volcano- and back-arc basin-hosted submarine hydrothermal vent fields investigated in this study. The geological framework of the different hydrothermal systems from this study and references to previous studies are summarized in Table 1 and section 2.

Keith et al., 2016; Zhang et al., 2020), the Eastern Manus basin (Satanic Mills, Roman Ruins; Wohlgemuth-Ueberwasser et al., 2015), and the Tonga arc (TA25 west; Choi et al., 2022) (Fig. 1). As such, the investigated hydrothermal systems comprise different island arcs and back-arc basins hosted vent fields that cover a wide range in host rock compositions (basalt to rhyolite), water depths (550 – 1900 m), fluid temperatures (22 – 380 °C), fluid salinities (300 – 650 mmol Cl), and fluid pH (2.8 – 7.9), which makes them representative for subduction-related submarine hydrothermal systems on the global-scale (Table 1).

The newly acquired and compiled published trace element data of pyrite and native S were separated into two groups: (1) hydrothermal systems affected by a MVP influx, and (2) those that lack evidence for a MVP component (Table 1). This classification is based on the results of previous studies, including sample mineralogy (e.g., abundance of high sulfidation minerals such as enargite or native S), fluid chemistry (e.g., high gas concentrations, low pH, low $\delta^{18}O$ isotopes), and low or negative $\delta^{34}S_{H2S}$ compositions of the fluids and/or the sulfide precipitates, which combined provide robust evidence for the influence of a MVP to the respective hydrothermal system and its related mineralization (e.g., de Ronde et al., 2011, 2015; Einaudi et al., 2003; Falkenberg et al., 2022; Herzig et al., 1998; Seewald et al., 2015, and references therein) (Table 1).

3. Methods

3.1. Sample preparation and mineralogy

Representative polished 1-inch blocks (n = 11) of hydrothermal sulfides and native S, from the aforementioned hydrothermally active volcanoes (Fig. 1), were petrographically examined to identify the different mineral phases (Table S1) and to avoid effects of mineral inclusions with respect to the following micro-analytical studies. The alteration mineralogy of representative sub-samples from hydrothermally altered and mineralized lavas was studied by X-ray diffraction (XRD) using a Siemens D5000 equipped with a Cu-long-fine-focus tube at 40 kV and 35 mA at the GeoZentrum Nordbayern. Scans were performed from 2 to 65° with a step size of 0.02° and 3 s measuring time per step. Semi-quantitative mineral abundances (as no amorphous phases were quantified) were calculated using the Rietveld-algorithm with the software *Profex* (Doebelin and Kleeberg, 2015).

Table 1

Compilation of the magmatic and hydrothermal key data of the investigated samples and the related subduction-related submarine hydrothermal systems. References: [1] Falkenberg et al. (2021), [2] Gartman et al. (2019), [3] Stoffers et al. (2006), [4] Keith et al. (2016), [5] de Ronde et al., 2011, [6] Kleint et al. (2019), [7] Stucker et al. (2022), [8] Fouquet et al. (1993), [9] Herzig et al. (1998), [10] Klose et al. (2021), [11] Falkenberg et al. (2022), [12] Klose et al. (2022), [13] Peters et al. (2021), [14] Kim et al. (2011), [15] Lupton et al. (2015), [16] Keith et al. (2021), [17] Schmidt et al. (2017), [18] Reeves et al., 2011, [19] McDermott et al., 2015.

Tectonic setting	Location	Vent field	Sample#	Sample-type	Latitude/ longitude	Depth [mbsl]	Host rock	Fluid T [°C]	Fluid pH	Fluid Cl [mmol]	Magmatic volatiles	Fluid boiling	Ref.
IA	Tonga	Niua South	SO263 29-ROV-3	Massive sulfide	15°09.89'S/ 173°34.46'W	1176	Rhyolite – dacite	259 – 318	3.1 – 7.9	531 – 646	no	yes	1, 2
	Tonga	Volcano 19 (caldera wall)	SO192/2 39R1046	Sulfide chimney	24°48.27'S/ 177.01.14'W	992	Basalt – basaltic andesite	112	4.6 – 6.1	/	/	yes	3, 4
	Tonga	Volcano 19 (cone)	SO192/2 49TVG-01	Sulfide chimney	24°48.45'S/ 176°59.58'W	548	Basalt – andesite	265 (clear fluid)	/	/	/	yes	3, 4
	Kermadec	Brothers (NW caldera)	SO135 52-DR-08	Altered lava	34°51.685'S/ 179°83.584'E	1462	Dacite	274 – 302 (black smoke)	2.8 – 7.5	283 – 762*	yes/no	yes	5, 6, 7
	Kermadec	Brothers (NW caldera)	SO135 66-DR-03	Native Sulfur	34' 52.784'S/ 179' 04.243'E	1313 – 1371	Dacite	/	/	/	yes/no	yes	5, 6, 7
BAB	VFR	Hine Hina	SO192/2 54R1049-07	Sulfide chimney	22°32.15'S/ 176°42.91'W	1831	Basalt – andesite	40 (diffuse)	/	/	yes	no	8, 9
	Lau	Maka	SO263 122-ROV-22	Massive sulfide	15°25.21'S/ 174°17.20'W	1535	Basalt	379* (black smoke)	4.5 – 5.4	309 – 490*	no	yes/no	10
	Lau	Niuatahi Southcentral	SO263 110-ROV-3	Sulfide chimney	15°23.249'S/ 173°59.890'W	1609	Rhyolite – dacite	267 – 334*	2.8 – 4.8*	288 – 319*	yes	yes	11, 12, 13
	Lau	Niuatahi Southcentral	SO263 82-ROV-1S	Native Sulfur	15°23.263'S/ 173°59.882'W	1618	Dacite	/	/	/	yes	yes	11, 12, 13
	Lau	Niuatahi Southwest	SO263 69-TVG-05	Altered lava	15°22.477'S/ 174°00.059'W	1420	Andesite – dacite	220 – 293*	3.4*	506*	yes/no	no	11, 12, 13
	Lau	Niuatahi Motutahi	DG-18–5	Altered lava	/	1244 – 1301	Dacite	22	/	/	yes	/	14, 15
	Lau	Niuatahi Motutahi	DG-18–5	Native S	/	1244 – 1301	Dacite	22	/	/	yes	/	14, 15
	Vate trough	Nifonea (Nif-6)	SO229 60-ROV-14	Sulfide chimney	18°07.402'S/ 169°31.313'E	1871	Basalt – basaltic andesite	350 – 360	/	/	no	yes	16, 17
	Manus basin	Satanic Mills	SO216 31-ROV-13B	Sulfide chimney	03°43.615'S/ 151°40.321'E	1691	Basalt – rhyolite	241 – 295*	2.4 – 2.6	414 – 517	yes	yes	18, 19

*Calculated endmember fluid compositions. Abbreviations: IA = island arc, BAB = back-arc basin.

3.2. Trace element and $\delta^{34}S$ micro-analysis

The major and minor element content (Fe, Cu, Zn, and S) of pyrite (n = 85) was determined by wavelength-dispersive X-ray spectrometry (WDS) with a focused beam, an acceleration voltage of 20 kV, and a beam current of 20nA by using a JEOL JXA-8200 Superprobe at the GeoZentrum Nordbayern. Count times for the WDS analysis were set to 20 and 10 s for peak and background measurements, respectively. The WDS was calibrated by the following standards: FeS_2 (Fe, S), $CuFeS_2$ (Cu), and ZnS (Zn). Stoichiometric calculations were used for data quality assurance and most analyses displayed an error <3 at. % with respect to the ideal stoichiometric pyrite composition. Pyrite measurements with analytical totals <98 wt.% and >102 wt.% were discarded.

Subsequently, in-situ $\delta^{34}S$ measurements of pyrite (n = 125) were performed by a CAMECA 1280-HR large geometry secondary ion mass spectrometer (SIMS) at the GeoForschungsZentrum (GFZ) in Potsdam. For the analysis, the 1-inch polished mounts were cleaned in a high-purity ethanol ultrasonic bath and then coated with 35 nm high-purity gold to assure electrical conductivity during the SIMS measurements. Polishing relief in each sample was <5 μm, as confirmed by white-light profilometry. A 1 nA $^{133}Cs^+$ primary ion beam was focused to a spot size of 10 μm with a total impact energy of 20 keV. Prior to data collection, each site of interest was sputtered for 70 s with a 20 μm raster in order to remove the gold coating, suppress any surface contaminants and to establish equilibrium sputtering conditions. Secondary ions were collected in multicollection mode using two Faraday cup detectors. The count rates on the ^{32}S isotope were on the order of $5.2 - 5.7 \times 10^8$ counts per second (cps) on the Balmat pyrite reference material (Crowe and Vaughan, 1996). Each analysis lasted 4 min including pre-sputtering, auto-centering, and data acquisition routines, which consisted of 20 integrations of 4 s each. The instrumental mass fractionation (IMF) and signal drift with time were monitored by repeated measurements throughout the analytical session on the Balmat pyrite reference material ($\delta^{34}S_{V-CDT}$ = 15.1 ‰; Crowe and Vaughan, 1996). No significant time-dependent drift was observed during the analytical session, which yielded a repeatability of ±0.08 ‰ (1 s, n = 45). We estimate, however, that the total analytical uncertainty on individual analyses is better than ± 0.7 ‰ (1 s), where the main sources of analytical uncertainty are the reported heterogeneities and assigned uncertainties on the bulk characterization of the Balmat pyrite (Crowe and Vaughan, 1996). Each SIMS spot was checked after analysis by reflected light microscopy and SEM to identify inclusions or fractures, which could affect the isotopic ratios. All S isotope values are presented in standard delta notation as per-mil difference relative to the S isotope composition of the Vienna Canyon Diablo Troilite (V-CDT) reference material (Ding et al., 2001).

Following the SIMS measurements, the same spots on the pyrite grains (n = 125) were analyzed for their trace element content (Co, Ni, Cu, Zn, Ge, As, Se, Mo, Ag, Cd, Sb, Te, Tl, Pb, and Bi) by LA-ICP-MS at the GeoZentrum Nordbayern. Additional pyrite grains (n = 47) and native S (n = 73) were also analyzed for their trace element content by the same method. The measurements were performed by a Teledyne Analyte Excite 193 nm laser coupled with an Agilent 7500c ICP–MS. The ICP–MS operated with a plasma power of 1190 W. Helium (0.9 l/min) and Ar (0.95 l/min) were used as carrier gases. Additionally, Ar acted as plasma (14.9 l/min) and auxiliary gas (0.9 l/min). A single spot ablation pattern with a frequency of 20 Hz and a fluence of 4.04 J/cm^2 was used. The total analysis time for each spot (beam diameter of 20 to 25 μm) was set to 55 s, including 20 s of gas blank analysis prior to ablation. Analytical precision and accuracy were monitored by the repeated analysis of the primary (MASS-1, PO724) and secondary (UQAC-FeS1) sulfide standards yielding a precision better than ± 7.0 % RSD for most elements except for Se (7.3 %), Ge (8.0 %), and Te (11.6 %), as well as an accuracy better than ± 9.5 % for all elements except for Te (13.4 %), Ag (19.9 %), and As (27.1 %). To monitor the instrument drift the sulfide standards were analyzed several times during an analytical day. Trace element contents and minimum detection limits were calculated by the Iolite4

(v.4.5.5.2) software package (Paton et al., 2011). Sulfur was chosen as the internal standard due to the lack of interferences in the analyzed element spectrum, since there is only a $^{16}O^{18}O$ interference on ^{34}S of about 1 % for all sulfides, which is produced from air (Sylvester, 2001). Intensity spikes in time-resolved LA-ICP-MS signals, induced by the ablation of micro-inclusion (Fig. S1), were filtered and discarded from the data reduction, but the occurrence of nanoparticles could not be resolved based on the used methodology (e.g., Börner et al., 2023; Deditius et al., 2011; González-Jiménez et al., 2022). Especially, the presence of e.g., telluride or sulfosalt inclusions was deliberately monitored which could influence the trace elements of interest in pyrite. The mainly smooth LA-ICP-MS ablation patterns (Fig. S1) suggest that most of the trace elements of interest occur as solid solution in our pyrite (e.g., Börner et al., 2023; Deditius et al., 2011). Trace element contents below the minimum detection limit of the newly and compiled literature data were replaced by 65 % of the minimum detection limit following the method by Palarea-Albaladejo and Martín-Fernández (2013). Further details about the analytical setup and methodology are provided in the supplementary material.

3.3. Native sulfur $\delta^{34}S$ analysis

Approximately 60 μg of native S separates (n = 2) were admixed with 300 – 500 μg of V_2O_5 and analyzed in tin capsules using a Flash EA IsoLink elemental analyzer interfaced to a ThermoScientific Delta V Advantage isotope ratio mass spectrometer (EA-IRMS) at the University of Münster. The repeatability, as determined by the repeated analysis of the V-CDT reference material (Ding et al., 2001), was better than ± 0.2 ‰ (2 s). Analyses of duplicates were better than ± 0.1 ‰ (2 s). All S isotope values are presented in standard delta notation as per-mil difference relative to the S isotope composition of the Vienna Canyon Diablo Troilite (V-CDT) reference material.

3.4. Trace element mapping by LA-ICP-MS

Quantitative trace element mappings of pyrite were performed at the MAGMA Lab of the TU Berlin using an Agilent 8900 ICP-MS/MS coupled to an Analyte Excite 193 nm excimer laser (Teledyne Photon Machines). Mass channels m/z = 34 (S), m/z = 57 (Fe), m/z = 66 (Zn), m/z = 72 (Ge), m/z = 75 (As), m/z = 95 (Mo), m/z = 121 (Sb), m/z = 125 (Te), and m/z = 208 (Pb) were recorded. The aerosol rapid introduction system ARIS (Teledyne Photon Machines) was used in combination with a low-volume adapter from Glass Expansion. Helium (99.999 %) was used as a carrier gas with a total flow rate of 0.95 l/min (0.5 l/min cell flow, 0.45 l/min cup flow) and small amounts (4 ml/min) of high-purity N_2 (99.999 %) were admixed to increase sensitivity. Grains were mapped with a 3 μm spot size at a fluence of 2 J/cm^2 by using a raster of unidirectional scans with no overlap between lines. A 2 s pause after each line was set to prevent memory effects. Dwell times, repetition rate, and dosage where optimized on test line scans on target grains to suppress aliasing and carry over effects, and to obtain a signal/noise ratio >10 for each mass channel. The STDGL reference material (Belousov et al., 2023) was used as the primary standard and MASS-1 (Wilson et al., 2002) and IMER5 (University of Adelaide) acted as secondary standards (Appendix A). Raw data processing was performed using the software package HDIP (Teledyne Photon machines). The external measurement uncertainty based on multiple line scans on MASS-1 and IMER5 was better than 5 % (2 RSE) for all elements. Internal measurement uncertainties based on a single line scan on STDGL were better than 4 % (2 RSE) and the accuracy was estimated to be <10 % (As, Se); <15 % (Te, Zn, Mo); and <30 % (Pb, Sb). Further details about the analytical setup and methodology are provided in the supplementary material.

4. Results

4.1. Mineralogy

The investigated samples include fragments of black smoker chimneys, massive pyrite-rich sulfides, pyrite-bearing hydrothermal altered lavas, and native S condensates (Table 1). The main sulfide minerals are sub- to euhedral pyrite, chalcopyrite, and sphalerite, as well as minor galena and chalcocite (Fig. 2A–K). Euhedral pyrite commonly occurs and precipitated directly in contact with fluid channels in most studied samples (Fig. 2C, J). Sulfosalts, such as enargite and tennantite-tetrahedrite, were observed at Hine Hina, Niuatahi Southcentral, and Satanic Mills (Fig. 2C). Kaolinite, alunite, and pyrophyllite (Table S1) occur in high-sulfidation alteration assemblages at the NW caldera vent

site of Brothers volcano, as well as at Niuatahi Southwest and Niuatahi Motutahi. Native S crusts on altered volcanic rocks were recovered from the Brothers NW caldera (Fig. 2L) and from Niuatahi Southcentral, where they are also associated with small native S globules (Fig. 2M). At Niuatahi Motutahi, native S occurs as a quenched mixtures of grey and yellow molten, crystalline, and globular S (Fig. 2N; Kim et al., 2011).

4.2. Coupled trace element and $\delta^{34}S$ data of pyrite and native S

The compiled published trace element data of pyrite from island arc volcanoes and back-arc basin hosted vent fields (n = 1249) show that Te contents are >1 µg/g in ~60 % of the pyrite analyses from hydrothermal systems characterized by a MVP influx, such as Hine Hina, Brothers NW caldera, and Niuatahi Motutahi (Fig. 3, Table 1). By contrast, only ~20
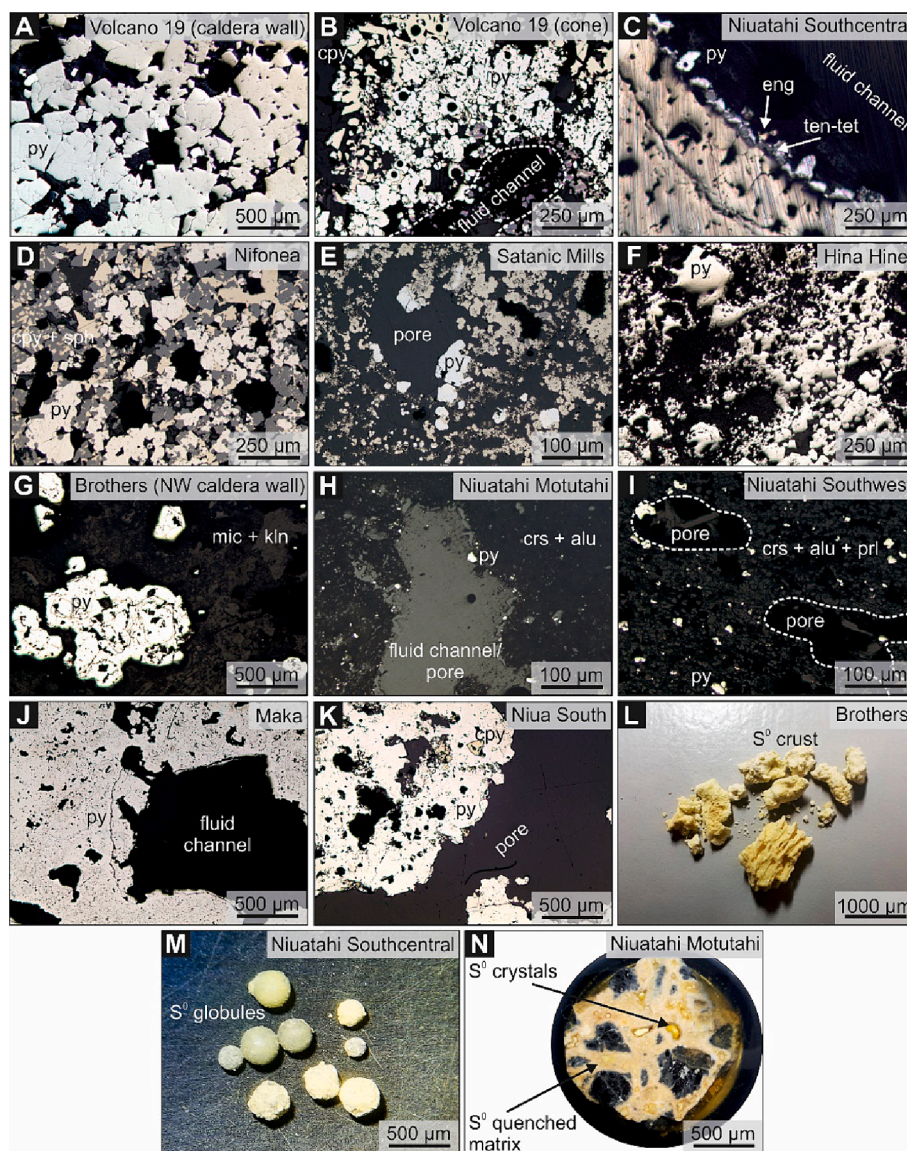

Fig. 2. Representative reflective light (plane polarized) images of petrographic features from the different vent sites. Samples from Volcano 19 (A, B), Niuatahi Southcentral (C), Nifonea (D), Satanic Mills (E), and Hine Hina (F) represent fragments of zoned black smoker sulfide-sulfate chimneys, where euhedral and subhedral (±anhedral) pyrite commonly occurs in direct contact to the central fluid channel. Samples from Brothers NW caldera (G), Niuatahi Motutahi (H), and Niuatahi Southwest (I) represent altered volcanic rocks with small disseminated subhedral to euhedral pyrite in a high-sulfidation alteration assemblage (e.g., kaolinite, pyrophyllite, and alunite) or euhedral pyrite precipitated in direct contact to fluid channels and/or pore spaces. Samples from Maka (J) and Niua South (K) are massive pyrite samples. (L) Native S crusts scrapped from altered volcanic rocks from the NW caldera wall at Brothers volcano. (M) Native S globules separated from alteration halos of volcanic rocks from Niuatahi Southcentral. (N) Quenched mixture of grey and yellow molten S, S crystals, S globules and altered host rock lavas from Niuatahi Motutahi (Kim et al., 2011). Abbreviations: py = pyrite, cpy = chalcopyrite, eng = enargite, ten-tet = tennantite-tetrahedrite, sph = sphalerite, mic = mica, kln = kaolinite, crs = cristobalite, alu = alunite, prl = pyrophyllite.
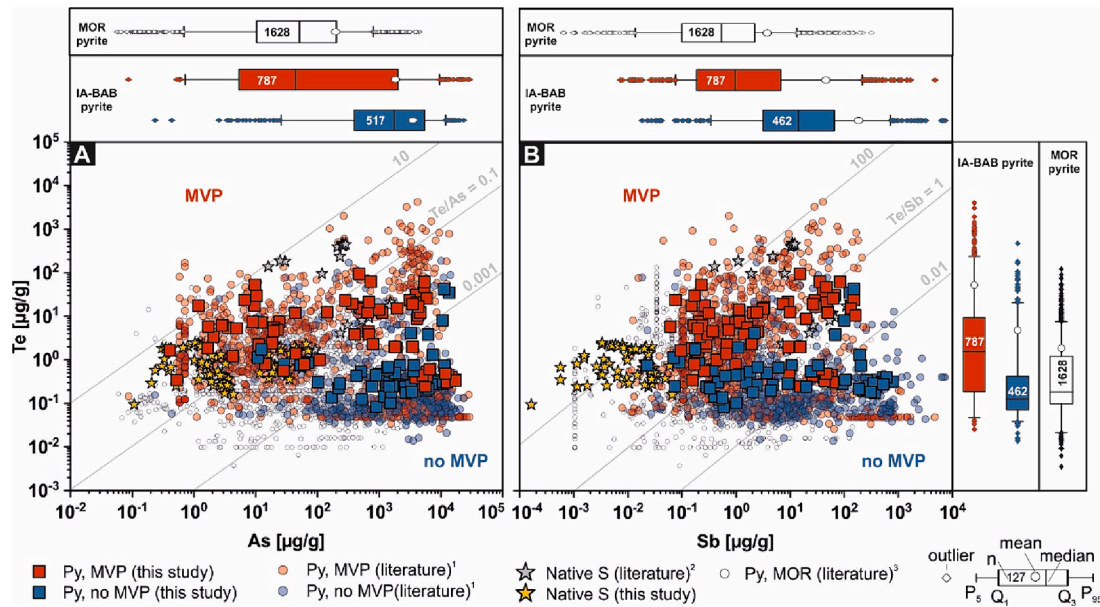
Fig. 3. Combined scatter and box-and-whisker plots of trace elements in pyrite and native S from this study and literature data. Based on previous results including mineralogy, fluid chemistry, in-situ trace element chemistry, and $\delta^{34}S$ composition, the different hydrothermal systems were classified as MVP and no MVP systems, which can be distinguished by distinct Te/As and Te/Sb values in pyrite and native S. Literature data includes pyrite[1] and native S[2] from island arc and back-arc basin-hosted (IA-BAB) vent fields (Choi et al., 2022; de Ronde et al., 2015; Falkenberg et al., 2021; 2022; Keith et al., 2016; Klose et al., 2021; Martin et al., 2022b; Wang et al., 2020; Wohlgemuth-Ueberwasser et al., 2015; Zhang et al., 2020) and pyrite from mid ocean ridge (MOR)[3] vent fields (Choi et al., 2023; Ding et al., 2022; Fan et al., 2022; Grant et al., 2018; Keith et al., 2016; Liao et al., 2021; Maslennikov et al., 2020; Melekestseva et al., 2018; 2020; Meng et al., 2020; Sahlström et al., 2023; Wang et al., 2017a; Wang et al., 2017b; Wang et al., 2018; Wang et al., 2022; Wohlgemuth-Ueberwasser et al., 2015; Yuan et al., 2018; Zhang et al., 2023). Abbreviations: MVP = magmatic volatile phase, MOR = mid-ocean ridge, IA = island arc, BAB = back-arc basin.

% of the compiled pyrite data from systems that lack evidence for a MVP influx show Te contents >1 μg/g (e.g., Maka South, Niua South, Nifonea; Table 1). In addition, ~36 % and ~50 % of the pyrite data from systems with a MVP influx have As and Sb contents >500 μg/g and >1 μg/g, respectively. Similar systematics were observed in the newly acquired trace element data (n = 172, Figs. 3 and 4). Despite some overlap, two distinct pyrite populations can be defined based on the combined dataset (i.e., new and compiled), where pyrite from MVP-influenced hydrothermal systems is characterized by higher Te/As and Te/Sb ratios compared to pyrite from MVP-free island arc and back-arc vent sites (Fig. 3). In addition, native S from Brothers NW caldera, Niuatahi Motutahi, and Niuatahi Southwest displays highly variable Te, As, and Sb contents, but shows consistently high Te/As and Te/Sb values that overlap with the pyrite data from the MVP-influenced hydrothermal systems (Fig. 3).

The in-situ $\delta^{34}S$ values of pyrite (Fig. 4, Fig. S2) range from -12.4 to 4.2 ‰ and are generally lower in hydrothermal systems that are influenced by a MVP (-5.3 ± 2.9 ‰, 1 s, n = 72) compared to those that lack any evidence of a MVP (1.0 ± 2.4 ‰, 1 s, n = 53). Native S separates from Brothers NW caldera revealed highly negative $\delta^{34}S$ values (-10.2 ± 0.1 ‰, 1 s, n = 2), which are comparable to those from Niuatahi Motutahi (-5.2 ± 2.5 ‰, 1 s, n = 4, Kim et al., 2011), Niuatahi South-central (-10.6 ‰, Peters et al., 2021), Daikoku volcano (-8.5 ± 0.1 ‰, 1 s, n = 9, de Ronde et al., 2015), and Nikko volcano (-7.1 ± 0.3 ‰, 1 s, n = 9, de Ronde et al., 2015). Our new in-situ $\delta^{34}S$ values of pyrite are consistently 2 to 3 ‰ lower than previously reported $\delta^{34}S$ values on mineral separates from the same locality (e.g., Hine Hina, Niuatahi Southcentral; Fig. S2). This is probably related to sulfate contamination with high $\delta^{34}S$ values in the previously analyzed sulfide separates. The data from Brothers NW caldera represents the only exception in this context, as our in-situ $\delta^{34}S$ data are higher than some of the related mineral separate values.

The coupled in-situ trace element and $\delta^{34}S$ data show a moderately negative correlation between $\delta^{34}S$ and Te (R = -0.47, p = 2.5^{-11}), as well as a moderately positive correlation between $\delta^{34}S$ and As (R = 0.53, p =

2.7^{-7}), as well as Sb (R = 0.41, p = 1.4^{-5}). Other volatile trace elements such as Bi (R = -0.38, p = 1.3^{-3}), Se (R = 0.05, p = 0.15), or Cu (R = -0.38, p = 5.1^{-6}) generally show a weaker correlation with $\delta^{34}S$ in pyrite compared to Te, As, and Sb (Fig. S3). An even stronger negative correlation was observed between the $\delta^{34}S$ composition of pyrite and the Te/As (R = -0.65, p = 2.7^{-13}) and Te/Sb (R = -0.60, p = 2.5^{-11}) ratios (Fig. 5). In addition, the inter-quartile range (IQR = $Q_3 - Q_1$) of the Te/As and Te/Sb ratios differs significantly between the two pyrite populations and discriminates the MVP-influenced hydrothermal systems from those without MVP influx (Figs. 3 to 5).

Based on our coupled $\delta^{34}S$ and trace element dataset, we define a quantitative threshold between the two pyrite populations at Te/As ~0.004 and Te/Sb ~0.6, which represents the average value between the upper quartile (Q_3) of the MVP-free and the lower quartile (Q_1) of the MVP-influenced pyrite group in the box and whisker plots (Fig. 5). We note that pyrite from mid-ocean ridge hydrothermal systems cannot be discriminated by its Te/As and Te/Sb ratios from those related to island arc and back-arc settings (cf. section 5.3). In addition, Te/As (~0.08 – 30) and Te/Sb (~0.7 – 1000) values vary by several orders of magnitude at a moderate $\delta^{34}S$ variability ($\delta^{34}S$ = -7.5 to -10.9 ‰) on the grain-scale, as observed in pyrite from Hine Hina, where the lowest $\delta^{34}S$ values coincide with the highest Te/As and Te/Sb values (Fig. 6A, Fig. S4). By contrast, pyrite from the NW caldera wall at Brothers volcano shows similar $\delta^{34}S$ values in the core ($\delta^{34}S$ = -0.5 ± 0.6 ‰, 1 s, n = 10) and rim ($\delta^{34}S$ = -1.0 ± 0.5 ‰, 1 s, n = 5) domains, but with distinctly higher Te/As and Te/Sb ratios at the rim (Fig. 6B, Fig. S5). This demonstrates that systematic variations in the $\delta^{34}S$ composition and trace element content of pyrite occur from the grain- to plate tectonic-scale between MVP-influenced and MVP-free hydrothermal systems in subduction-related settings.
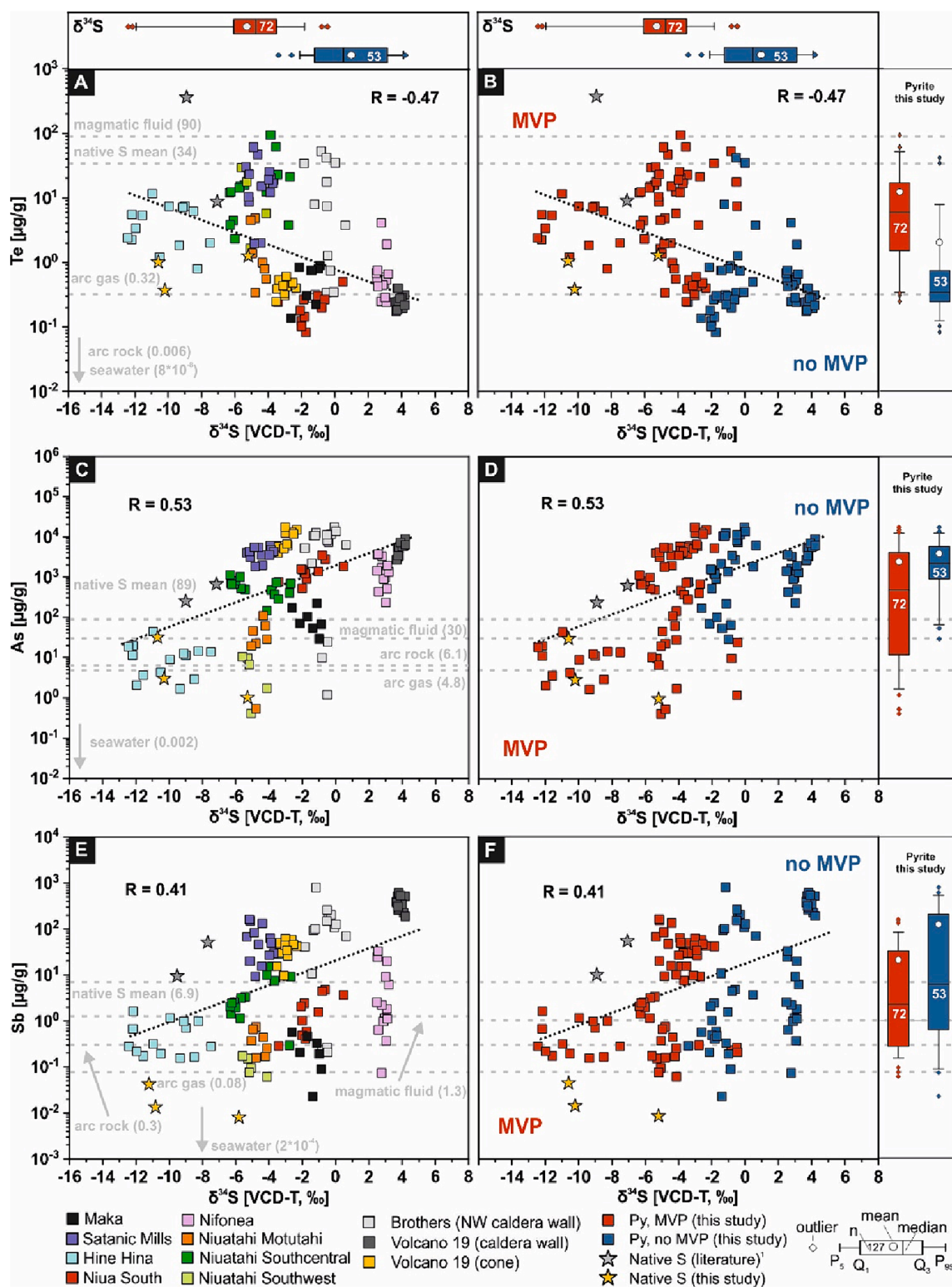
Fig. 4. Combined scatter and box-and-whiskers plots of in-situ LA-ICP-MS trace element contents of pyrite coupled with in-situ SIMS $\delta^{34}S$ values. (A, B) Tellurium shows a moderate negative (R = -0.47) correlation with $\delta^{34}S$, whereas (C, D) As (R = 0.53) and (E, F) Sb (R = 0.41) show moderate positive correlations. Average Te, As, and Sb contents of different reservoirs such as magmatic fluid (Pudack et al., 2009), native S (this study, Ronde et al. 2015), volcanic island arc gases (Mandon et al., 2020; Zelenski et al., 2021), island arc volcanic rocks (Zelenski et al., 2021), and seawater (Sohrin and Bruland, 2011) are shown for comparison. Abbreviations: MVP = magmatic volatile phase.
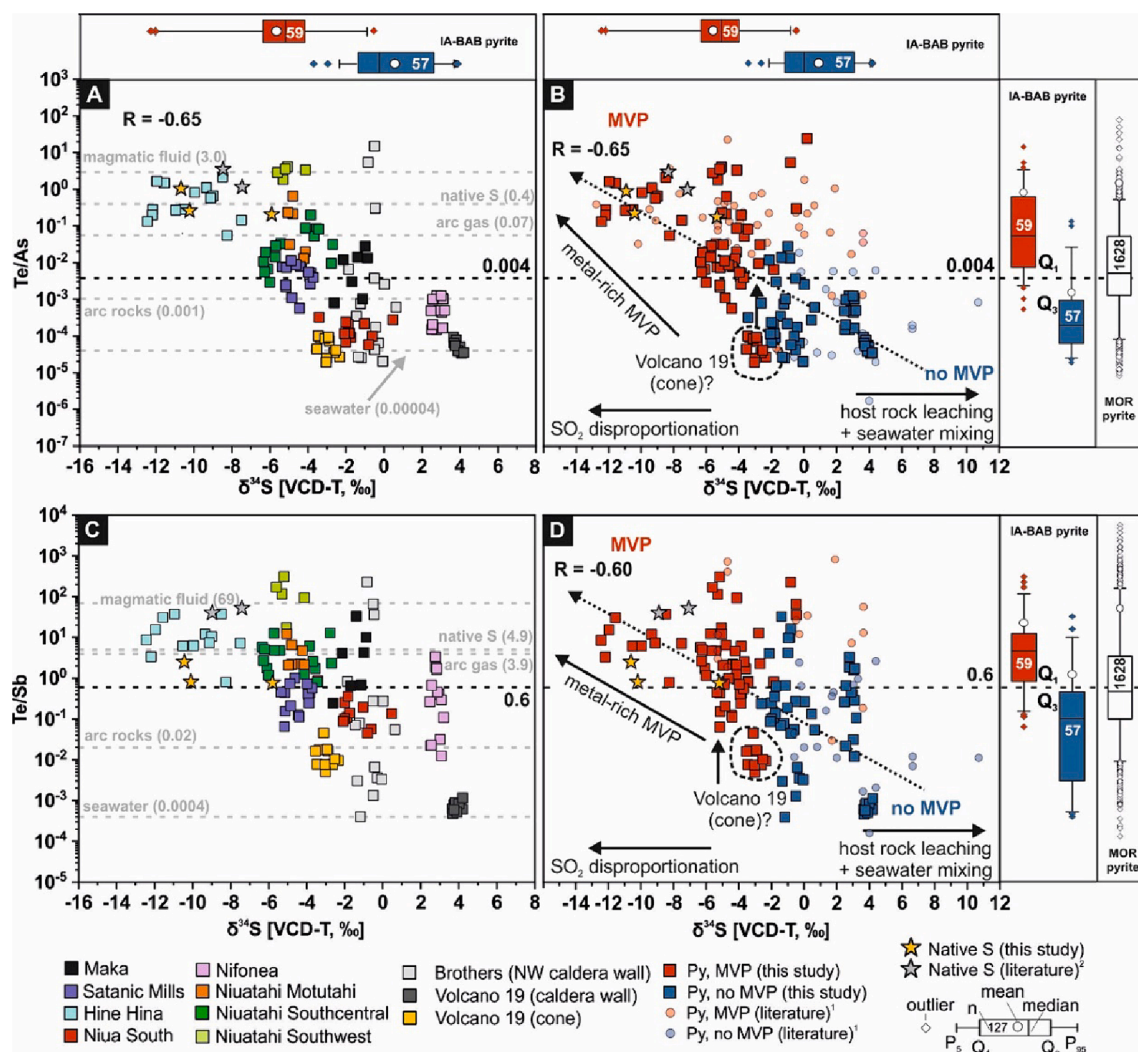
Fig. 5. Combined scatter and box-and-whiskers plots of coupled trace element ratios and $\delta^{34}S$ values in pyrite and native S. (A, B) Te/As (R = -0.65) and (C, D) Te/Sb (R = -0.60) show a negative correlation with $\delta^{34}S$. The quantitative threshold for distinguishing the two pyrite populations is defined by the average Te/As ($\sim$0.004) and Te/Sb ($\sim$0.6) ratio between the Q_3 of the lower group and Q_1 of the upper group. Published pyrite data is shown as the average trace element ratio and $\delta^{34}S$ value of each sample (B, D). If this was not possible on the same sample, the average trace element ratio and average $\delta^{34}S$ value of the whole vent field were used. Pyrite from Volcano 19 (cone) was excluded in the box-and-whisker plots as most Te contents are below the MDL (see text for details). Note: Pyrite from the NW caldera wall of Brothers is shown as MVP-influenced (rims) and not MVP-influenced (cores) in (B) and (C) based on the zonation observed in the grains (Fig. 6) and the mixing model in Fig. 7. The grey dashed lines show the average Te/As and Te/Sb of magmatic fluids, native S, seawater, island arc rocks, and volcanic island arc gas (same references as in Fig. 4). Literature data includes pyrite[1] (Aoyama et al., 2014; Choi et al., 2022; Falkenberg et al., 2021; 2022; Herzig et al., 1998; Keith et al., 2016; Klose et al., 2021; Lüders et al., 2001; Martin et al., 2022a; Martin et al., 2022b; McDermott et al., 2015; Wang et al., 2020; Wohlgemuth-Ueberwasser et al., 2015; Zhang et al., 2020), native S[2] (de Ronde et al., 2015) and MOR[3] pyrite (same references as in Fig. 3). Abbreviations: MVP = magmatic volatile phase, MOR = mid-ocean ridge, IA = island arc, BAB = back-arc basin.

5. Discussion

5.1. Trace element and $\delta^{34}S$ characteristics of magmatic volatiles

Cooling of a MVP to temperatures <400 °C results in S isotope fractionation during SO_2 disproportionation, which significantly reduces the $\delta^{34}S_{H2S}$ value of the fluid and leads to characteristically low and negative $\delta^{34}S$ values in the related sulfide precipitates (Herzig et al., 1998; Kusakabe et al., 2000; McDermott et al., 2015). Consequently, pyrite from Hine Hina, Niuatahi, Satanic Mills, and the Volcano 19 cone site that is characterized by $\delta^{34}S$ values below -2 ‰, provides strong evidence for MVP influx to these hydrothermal systems (Fig. 4). The lowest $\delta^{34}S$ values in pyrite were found at Hine Hina ($\delta^{34}S = -10.2 \pm 1.7$ ‰, 1 s, n = 14), suggesting that they formed by a fluid dominated by magmatic H_2S derived from SO_2 disproportionation (c.f., section 5.3). Alternatively, negative $\delta^{34}S$ signatures in pyrite can be produced by

bacterial sulfate reduction (Habicht and Canfield, 1997; Nozaki et al., 2021). However, we exclude a biogenic S source for the studied vent sites due to only minor sedimentary layers, which would be necessary to provide a suitable habitat for microbial life, and which could be an additional source for extensive leaching of reduced S derived from bacterial seawater sulfate reduction. Furthermore, the high fluid temperatures typically observed in the center of the sulfide chimneys, that were partly measured on the seafloor (>240 °C, except Volcano 19 caldera wall; Table 1) and recorded in the associated high sulfidation mineral assemblages (e.g., Einaudi et al., 2003) likely suppress bacterial activity. In addition, multiple S isotope data ($\Delta^{33}S$, $\delta^{34}S$) of vent fluids from Niua South, Brothers NW caldera, Niuatahi volcano, and Maka indicate that in these currently active and young venting systems the effect of bacterial sulfate reduction is negligible (Gartman et al., 2019; Peters et al., 2021).

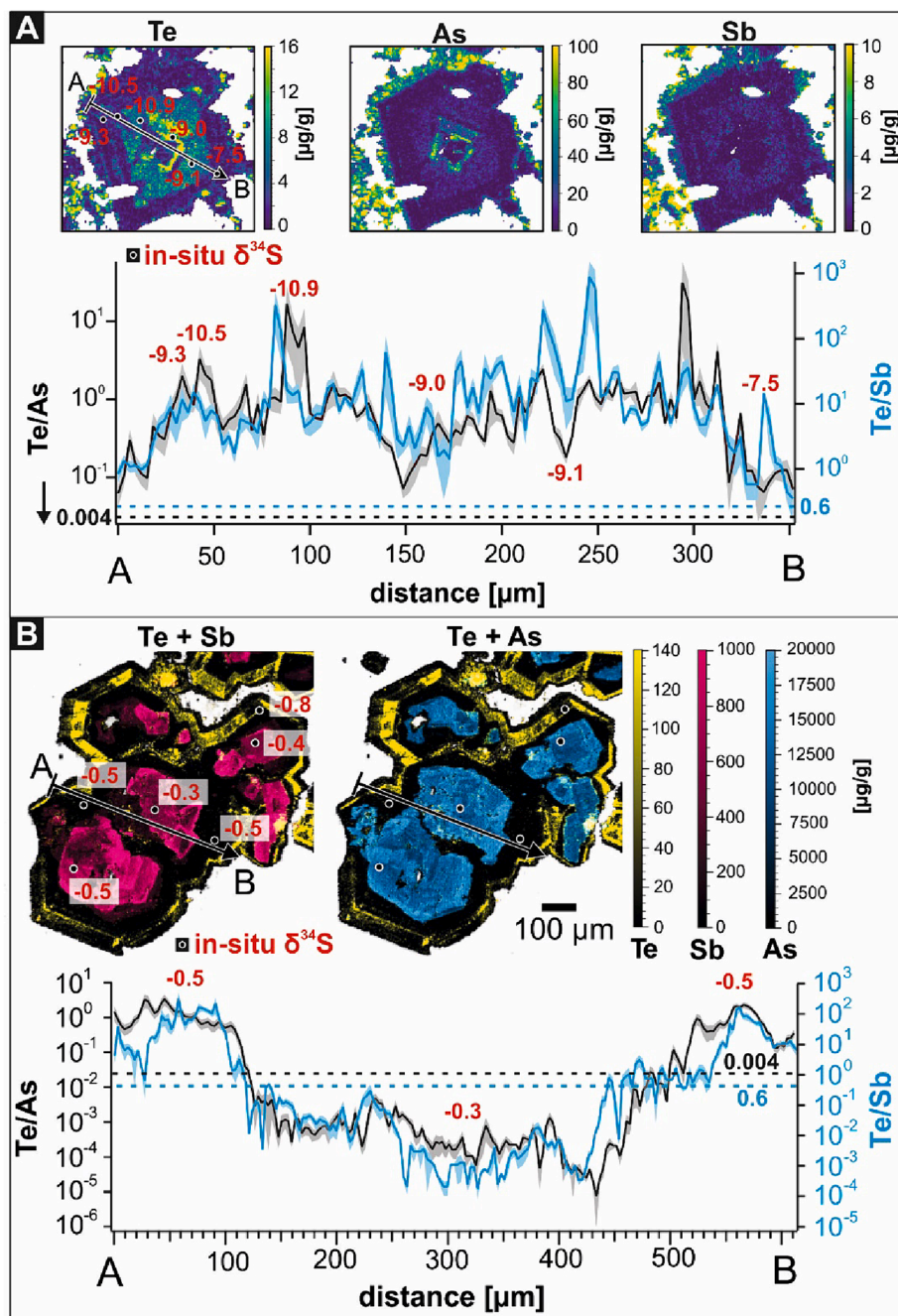By contrast, consistently positive $\delta^{34}S$ values in hydrothermal pyrite

Fig. 6. Trace element LA-ICP-MS maps (pyrite pixel only), Te/As and Te/Sb intra-grain profiles and related δ^{34}S spots by SIMS. (A) High Te/As and Te/Sb above the MVP threshold correlate with lower δ^{34}S values in the studied pyrite grain from Hine Hina. (B) Te-As and Te-Sb decoupling in pyrite from Brothers NW caldera. Pyrite rims are characterised by higher Te/As and Te/Sb than the cores at similar δ^{34}S values.

are commonly related to seawater-dominated fluids without a MVP component, as observed at Nifonea volcano and the Volcano 19 caldera wall vent site (>2 ‰, Fig. 4), where most of the S was leached from the host rocks or was derived from thermochemical seawater sulfate reduction (McDermott et al., 2015; Ono et al., 2007). Based on a two-component mixing model (Ono et al., 2007) between the δ^{34}S composition of modern seawater (~21.2 ‰, Tostevin et al., 2014) and island arc (5.0 ± 3.9 ‰, 1 s, n = 125; Ueda and Sakai, 1984; Woodhead et al., 1987; Alt et al., 1993; de Hoog et al., 2001) and/or back-arc volcanic rocks (δ^{34}S = 1.1 ± 0.5 ‰, 1 s, n = 10; Alt et al., 1993), we estimate that up to 14 % of the total S content in pyrite from Nifonea volcano and Volcano 19 caldera wall was derived from thermochemical seawater sulfate reduction, suggesting a significant S contribution from host rock

leaching (up to 86 %).

Pyrite from Niua South, Maka, and Brothers NW caldera shows positive and negative δ^{34}S values ranging from -2 ‰ to 2 ‰, which suggests that S was derived from multiple sources, including host rock leaching, thermochemical seawater sulfate reduction, and magmatic SO_2 disproportionation (Fig. 4 and Fig. S2; de Ronde et al., 2011; Falkenberg et al., 2021; Klose et al., 2021). At Brothers volcano, partly negative δ^{34}S values derived from sulfide separates (-5.6 to 3.0 ‰; de Ronde et al., 2005, 2011) and pyrite micro-analysis (-13.3 to 3.8 ‰; Martin et al., 2022b), in combination with high CO_2, SO_4^{2-}, and H_2S concentrations, low pH, and negative δD and $\delta^{18}O_{H2O}$ values in hydrothermal fluids (de Ronde et al., 2011; Kleint et al., 2019) verify a MVP contribution to this hydrothermal vent site. Kaolinite, alunite, and

pyrophyllite alteration (Table S1) together with the occurrence of enargite (Fig. 2C) and native S (Fig. 2L–M) at Brothers NW caldera are also indicative of high-sulfidation conditions related to a MVP influx (Berkenbosch et al., 2019; de Ronde et al., 2011). Similar mineral assemblages with enargite and native S were also observed at Hine Hina (Herzig et al., 1998) and Niuatahi (Falkenberg et al., 2022), where the δ^{34}S values are consistently <2 ‰ (Fig. 5), which also agrees with a MVP contribution. By contrast, such mineral assemblages are lacking at Maka, Niua South, Nifonea volcano, and Volcano 19 caldera wall, where the δ^{34}S values of pyrite are consistently positive (>2 ‰), thereby revealing that these systems are primarily controlled by seawater-dominated fluids without a MVP component (Schmidt et al., 2017; Gartman et al., 2019; Falkenberg et al., 2021; Keith et al., 2021; Klose et al., 2021). Consequently, the trace element data of pyrite and native S were assigned to (1) hydrothermal systems with a MVP (δ^{34}S = -5.3 ± 2.9 ‰, 1 s, n = 72) and (2) without a MVP influx (δ^{34}S = 1.0 ± 2.4 ‰, 1 s, n = 53), as reflected by the distinct δ^{34}S signatures, sample mineralogy, and chemistry of the vent fluids, which is conclusive with findings from previous studies at these vent sites (Table 1). Thus, our dataset is representative for a continuum from magmatic fluid- to seawater-dominated subduction-related submarine hydrothermal systems, since the δ^{34}S values (Fig. S2) and the Te, As, and Sb contents in pyrite (Fig. 3) cover most of its natural variability in this geodynamic environment.

Changes in the Te/As and Te/Sb values of pyrite at low δ^{34}S values (<-2 ‰), i.e., in the MVP-influenced group, are indicative of Te fractionation from other volatile elements like As and Sb during magma degassing (Fig. 5). This agrees with the extreme volatility of Te, as indicated by a volatile-melt partition coefficient ($Kd_{volatile-melt}$) of ~ 77, which is at least an order of magnitude higher than that of As ($Kd_{volatile-melt}$ ~ 0.8) and Sb ($Kd_{volatile-melt}$ ~ 3) (Edmonds et al., 2022; Zelenski et al., 2021). This makes Te particularly sensitive for tracking a MVP contribution to hydrothermal systems (Berkenbosch et al., 2019; Falkenberg et al., 2022; Grosche et al., 2023; Wohlgemuth-Ueberwasser et al., 2015), leading to higher Te/As and Te/Sb ratios in fluids and the related pyrite precipitates in MVP-influenced systems (Fig. 5). The application of Te/As (R = -0.65) and Te/Sb (R = -0.60) ratios enhances the correlation with δ^{34}S in pyrite by 38 and 28 %, respectively, compared to using the absolute Te contents (R = -0.47). This highlights the usefulness of trace element ratios compared to absolute trace element contents (Figs. 4 and 5). Thus, we conclude that trace element ratios further have the advantage that the signature of other hydrothermal processes like temperature changes and fluid boiling are reduced in the geochemical record, and thus can better preserve the potential signature of MVP influx (cf. section 5.2). The high volatility of Te can also explain why such systematic MVP signatures are not observed for other trace elements with lower volatility, such as Bi ($Kd_{volatile-melt}$ ~ 12) or Cu ($Kd_{volatile-melt}$ ~ 0.1) (Fig. S3; Zelenski et al., 2021). Selenium ($Kd_{volatile-melt}$ ~ 52) is nearly as volatile as Te ($Kd_{volatile-melt}$ ~ 77) and high contents of Se has previously been thought to record MVP influx in ancient VMS systems (Layton-Matthews et al., 2013; Martin et al., 2020). However, no systematic relation of Se with the δ^{34}S composition of pyrite is recorded in our dataset (R = 0.05, Fig. S3). Similarly, hydrothermal pyrite from the ancient MVP-influenced Mala VMS system in the Troodos ophiolite (Cyprus) also lacks any systematic relation between the Se and δ^{34}S composition, which has been related to hydrothermal reworking during system maturation (Martin et al., 2022a). It can be excluded that hydrothermal reworking caused significant geochemical variations in our dataset by remobilization and reprecipitation reactions, because our study focused on euhedral pyrite from the inner zone of the chimney wall where pyrite growth likely occurred in a near-equilibrium state with the fluid (Fig. 2). These pyrites thus represent the youngest precipitates of the hydrothermal system, for which reason extensive hydrothermal reworking is unlikely. Instead, we attribute the unsystematic Se variation with respect to MVP influx to the strong temperature control on the Se solubility in fluids and its

incorporation into pyrite as shown by multiple studies in active and ancient hydrothermal systems (e.g., Auclair et al., 1987; Butler and Nesbitt, 1999; Grosche et al., 2024; Huston et al., 1995; Keith et al., 2018; Maslennikov et al., 2009). Hence, cooling during fluid upflow, discharge, and sulfide precipitation likely overprint potential earlier MVP signatures with respect to Se.

Metal-rich native S, which forms due to the condensation of a MVP into seawater (de Ronde et al., 2015; Kim et al., 2011), provides evidence for the transport of metals by a MVP to the seafloor and its contribution to the metal endowment of submarine hydrothermal systems (de Ronde et al., 2015; Kim et al., 2011; Yang and Scott, 2006). The magmatic origin of native S is supported by its highly negative δ^{34}S values (down to -10.6 ‰), as observed at Brothers NW caldera (this study), Niuatahi Motutahi (Kim et al., 2011), Niuatahi Southcentral (Peters et al., 2021), and at Daikoku and Nikko volcano (de Ronde et al., 2015). This is consistent with S isotope fractionation during magmatic SO_2 disproportionation and subsequent condensation of the fluid into seawater (Fig. S2; Kusakabe et al., 2000; McDermott et al., 2015). Importantly, the native S samples are characterized by high Te/As (>0.004) and Te/Sb (>0.6) ratios, which show Te/As and Te/Sb ratios comparable to pyrite from the MVP-influenced systems (Figs. 3 and 4), and are thus assumed to record the trace element signature of a MVP. This is conclusive with comparably high Te/As (~3.0) and Te/Sb (~69) values of magmatic fluids measured in primary single-phase and intermediate-density fluid inclusions from the Nevados de Famatina Cu-Mo-Au porphyry deposit (Fig. 4; Pudack et al., 2009). Similarly, volcanic gases from arc volcanoes also show elevated Te/As (~0.07) and Te/Sb (~3.9) values (Edmonds et al., 2018; 2022; Zelenski et al., 2021) that are above the proposed threshold for MVP influx (Te/As ~ 0.004, Te/Sb ~ 0.6). By contrast, the Te/As and Te/Sb values of degassing-corrected volcanic arc rocks (Te/As = 0.001, Te/Sb = 0.02; Zelenski et al., 2021) and of seawater (Te/As = 0.00004, Te/Sb = 0.0004, Sohrin and Bruland, 2011) are several orders of magnitude lower (Fig. 5), indicating that host rock leaching and seawater mixing cannot result in high Te/As (>0.004) and Te/Sb (>0.6) values in native S condensates and hydrothermal pyrite from subduction-related settings.

Due to the lack of pyrite-fluid partition coefficients ($Kd_{pyrite-fluid}$) for Te and the generally complex incorporation mechanism of Te in pyrite (e.g., Börner et al., 2023), potential trace element fractionation effects during pyrite precipitation on the Te/As and Te/Sb ratios cannot entirely be excluded. Furthermore, we acknowledge that MVP influx does not only increase the metal budget (e.g., Te concentration) of the hydrothermal fluid but can also change its physicochemical conditions. However, the effect of these changing fluid conditions on the $Kd_{pyrite-fluid}$ value of Te and other elements (e.g., As, Sb, or Se) remains unknown. Nevertheless, the link presented here between Te/As and Te/Sb ratios and the δ^{34}S isotope composition of pyrite, native S, arc volcanic gas, and magmatic fluids provides strong empirical evidence that these trace element ratios are sensitive to MVP influx into submarine hydrothermal systems and are not just the result of natural coincidence.

5.2. Paragenetic and fluid effects on Te/As and Te/Sb in pyrite

Black smoker chimneys are characterized by strong physicochemical gradients (e.g., temperature) from core to rim, which is also reflected by the mineralogy and the chemical composition of associated sulfides (Berkenbosch et al., 2012; Berkenbosch et al., 2019; Butler and Nesbitt, 1999; Falkenberg et al., 2021; Keith et al., 2016; Meng et al., 2019). In this study, we deliberately used sub- to euhedral pyrite, which formed in direct contact with the fluid channel in the center of the chimney structure or in pore spaces of massive sulfide aggregates (e.g., Fig. 2A, C, E), suggesting a formation at near-endmember fluid conditions with little seawater influence (Berkenbosch et al., 2012; Meng et al., 2019). Consequently, paragenetic effects during the fluid evolution should have only a minor control on the related pyrite composition (Butler and Nesbitt, 1999; Falkenberg et al., 2021; Meng et al., 2019). Similarly,

disseminated pyrite that occurs in contact to pore space in lavas with a high-sulfidation alteration assemblage (e.g., kaolinite; Table S1) are suggested to be directly related to the acidic high-sulfidation fluids (Fig. 2G–H).

Temperature and salinity have a strong control on the metal solubility in hydrothermal fluids, and thus also control the trace element contents of associated sulfide precipitates (Metz and Trefry, 2000; Reed and Palandri, 2006). However, we suggest that the selected trace element ratios are influenced but not primarily controlled by fluid temperature variations, as indicated by comparable Te/As and Te/Sb ratios in pyrite from vent sites with distinct fluid temperatures, such as Satanic Mills (241 – 295 °C) and Maka (~379 °C) (Fig. 5). This is further supported by the only weak correlation of Te/As (R = 0.27) and Te/Sb (R = 0.34) with temperature-sensitive trace element ratios like Se/Tl, that typically increases in pyrite with increasing fluid temperature (Falkenberg et al., 2021; Grosche et al., 2024; Maslennikov et al., 2009). Even though it is theoretically possible that a Se influx from a MVP could have influenced the temperature-sensitive Se/Tl ratio, we find no evidence for a strong correlation between Se/Tl and $\delta^{34}S$ (R = 0.13). Furthermore, the highest Se/Tl ratios were observed in pyrite from Nifonea volcano and Maka, which host the vent fields with the highest fluid temperatures (>360 °C, Table 1) and is therefore consistent with our interpretation. Hence, we conclude that temperature variations in the range of the measured fluid temperatures (240 – 380 °C, Table 1) have only a minor effect on the Te/As and Te/Sb ratio in pyrite compared to the influx of a MVP. Thus, the large variation over several orders of magnitude in these ratios that correlate with the $\delta^{34}S$ values, are likely indicative of variable MVP influx (Table 1).

Fluid salinity typically changes in response to fluid boiling and mixing, which is a common process in shallow (<2000 m) subduction-related submarine hydrothermal systems (Monecke et al., 2014; Schmidt et al., 2017; Stoffers et al., 2006). As such, fluid boiling can also drastically alter the trace element budget of the sulfide-forming fluid by element partitioning between the vapor and liquid phase (Pokrovski et al., 2013). Tellurium seems to have a stronger affinity to the vapor phase (Grundler et al., 2013) than As and Sb during fluid boiling (Pokrovski et al., 2013), which suggests that vapor-rich fluids and related sulfide precipitates are likely characterized by relatively high Te/As and Te/Sb values. However, as neither Te nor As or Sb occur dominantly as Cl-complexes in aqueous solutions, and instead mostly form oxy or hydroxide complexed species, such as H_2TeO_3, $As(OH)_3$, and $Sb(OH)_3$ (Brugger et al., 2016; Grundler et al., 2013; Pokrovski et al., 2013), salinity variations induced by fluid boiling likely do not significantly influence the solubility of Te, As and Sb. However, if the Te/As and Te/Sb ratios in pyrite were influenced by fluid boiling and vapor–liquid fractionation, then low salinity vapor-rich fluids, such as those from Niuatahi Southcentral (288 – 319 mmol Cl), should precipitate pyrite with higher Te/As and Te/Sb values than those of near seawater salinity (545 mM Cl; Schmidt et al., 2017) like at Niuatahi Southwest (~506 mmol Cl; Klose et al., 2022). Previous results on the trace element composition of pyrite from sulfide chimneys from the different vent sites at Niuatahi volcano suggest that the Te/As and Te/Sb variations are the result of both, a MVP influx and boiling-induced element fractionation (Falkenberg et al., 2022). Here, we investigated sub- to euhedral pyrite from additional samples from Niuatahi volcano, namely volcanic rocks altered at high-sulfidation conditions, which yielded contrasting results in comparison to Falkenberg et al. (2022). Our new data show that pyrite from Niuatahi Southwest is characterized by higher Te/As and Te/Sb ratios than pyrite from Niuatahi Southcentral (Fig. 5) despite higher fluid salinities at the former compared to the latter site (Table 1). This observation thus contradicts with a potential boiling-induced Te/As and Te/Sb variation between these two vent sites at Niuatahi volcano. Hence, it is more likely that these variations are the result of variable MVP influx, as supported by the variable but negative in-situ $\delta^{34}S$ values at Niuatahi Southwest (-5.6 to -4.1 ‰) and Niuatahi Southcentral (-6.3 to -2.7 ‰). Irrespective of the discrepancy between our results and those

of Falkenberg et al. (2022), both studies show that the Te/As (and Te/Sb) ratios vary due to MVP influx even in boiling hydrothermal environments. In addition, boiling and non-boiling fluids sampled at Niua South (Gartman et al., 2019) show comparable Te/As (~0.002 – 0.003) values despite distinct fluid salinities (453 – 646 mmol Cl), further supporting our conclusion that fluid boiling does not majorly change the Te/As ratio of hydrothermal fluids and related pyrite precipitates. We note that Gartman et al. (2019) did not report any Sb concentrations for boiling- and non-boiling fluid at Niua South, so that a direct comparison of similar Te/Sb ratios in boiling and non-boiling fluids is not possible. However, the chemical similarity and the relatively low but comparable vapor–liquid partitioning coefficient of Sb and As suggest a similar relative behavior of the Te/Sb and Te/As ratio in boiling hydrothermal fluids (Pokrovski et al., 2013). Furthermore, we note that pyrite grains with typical boiling-induced textures, such as zones of high porosity (Román et al., 2019), were deliberately excluded from the micro-analysis to minimize the potential effect of fluid boiling on our dataset. Therefore, although fluid boiling was observed at the seafloor at the investigated vent sites (Table 1), we suggest that differences in the Te/As and Te/Sb values in the studied euhedral pyrites are not primarily controlled by fluid boiling.

Unexpectedly, pyrite from the Volcano 19 cone vent site shows low Te contents that are mostly below the minimum detection limit (<0.5 µg/g) at relatively high As and Sb contents, leading to abnormally low Te/As and Te/Sb ratios, despite their low $\delta^{34}S$ values (Fig. 5). This could be due to extensive subseafloor Te-rich but As- and Sb-poor precipitation, which would deplete the fluid in Te relative to As and Sb (Fig. 4). This subseafloor precipitation process results in the discharge of clear fluids, which could be enhanced by the shallow water depth of the cone vent site (~550 m) at Volcano 19 (Keith et al., 2016; Stoffers et al., 2006). By contrast, most black smoker-type fluids that occur at greater water depth, such as at the Brothers NW caldera (1310 – 1460 m), Maka (1535 m), and Niua South (1170 m), did not lose most of their metal budget in the subseafloor (de Ronde et al., 2011; Falkenberg et al., 2021; Klose et al., 2021). We conclude that, in subduction-related vent fields the differences in the Te/As and Te/Sb values in inclusion-free and sub- to euhedral pyrite, which are free of fluid boiling-related textures (Román et al., 2019) and that precipitated at near-endmember conditions are influenced but not primarily controlled by physicochemical fluid parameters (e.g., temperature, salinity). Instead, these ratios can rather record the source signature of the fluid, such as a MVP influx which outweighs other hydrothermal processes.

5.3. Fingerprinting MVP influx from the grain- to plate tectonic-scale

The highly negative $\delta^{34}S$ values ($\delta^{34}S$ = -10.2 ± 1.7 ‰, 1 s, n = 14, Fig. 4) in pyrite from Hine Hina are consistent with the SO_2 disproportionation model by McDermott et al. (2015), suggesting a pyrite formation from MVP-dominated fluids, as also indicated by the high Te/As (0.7 ± 0.6, 1 s, n = 14) and Te/Sb (13.4 ± 12.5, 1 s, n = 14) ratios. Accordingly, zones of higher Te/As and Te/Sb correlate with highly negative $\delta^{34}S$ values on the grain-scale in pyrite from Hine Hina (Fig. 6A). This demonstrates that our approach is not only capable to distinguish different hydrothermal systems with variable MVP influx on the plate tectonic-scale in subduction-related settings (Fig. 5), but also records short-term variations of MVP influx as preserved on the grain-scale in pyrite (Fig. 6).

Similarly, pyrite from Brothers NW caldera shows a wide intra-grain Te/As and Te/Sb variability, with values above the proposed MVP threshold (Te/As > 0.004, Te/Sb > 0.6) at the rim compared to lower values in the core domains of single grains (Fig. 6B). We attribute this to temporal variations in MVP influx, reflecting seawater-dominated conditions during early pyrite growth (i.e., core) followed by a stage of more significant MVP influx causing the elevated Te/As and Te/Sb ratios in the pyrite rims. This conclusion is supported by similar Te/As and Te/Sb ratios of the pyrite rims from Brothers NW caldera and of pyrite derived

from acid sulfate alteration assemblages (pyrophyllite + natroalunite + smectite + plagioclase) from the Brothers cone vent site (Fig. S6) that were interpreted to be the result of a strong MVP influx, as indicated by their low $\delta^{34}S$ values (-12.2 to 0.3 ‰; Martin et al., 2022b). Accordingly, the low Te/As and Te/Sb ratios in the pyrite core domains overlap with the pyrite composition from the chlorite alteration zone at Brothers NW caldera, therefore confirming a precipitation from a seawater-dominated fluid (Martin et al., 2022b). In agreement with our conclusion, a variable MVP contribution to the Brothers NW caldera vent field has also been suggested by mineral zoning and trace element mapping of chimney fragments (Berkenbosch et al., 2019), time-series of hydrothermal fluids (Stucker et al., 2022), high-sulfidation acid alteration assemblages (Martin et al., 2023b), negative $\delta^{34}S$ compositions of pyrite (de Ronde et al., 2011; Martin et al., 2022b), and pyrite trace element mappings (Martin et al., 2023a).

Despite the variable Te/As and Te/Sb values between the core and rim domains in pyrite from Brothers NW caldera, the $\delta^{34}S$ composition is comparable throughout the grain, considering the analytical uncertainty (cf. section 3.2). Thus, a process is required that decouples Te/As and Te/Sb from $\delta^{34}S$ on the grain-scale in pyrite from the Brothers NW caldera vent site. Fluid boiling can shift the $\delta^{34}S_{H2S}$ composition of a fluid to lower values, which results in highly negative $\delta^{34}S$ values down to -15 ‰ in the related sulfide precipitates (González-Partida et al., 2005; McKibben and Eldridge, 1990; Schaarschmidt et al., 2021), including significant $\delta^{34}S$ intra-grain variabilities (Börner et al., 2022; McKibben and Eldridge, 1990). Since our $\delta^{34}S$ values in the pyrite grain from Brothers NW caldera are neither particularly negative nor do they show a significant intra-grain variability, we exclude fluid boiling as a reasonable process that could decouple the $\delta^{34}S$ signature from the Te/As and Te/Sb ratios (Fig. 6B). Alternatively, fluid-seawater mixing and thermochemical seawater sulfate reduction in the subseafloor can cause significant S isotope variations, which may modify the signature of a MVP in the hydrothermal fluids and the related pyrite precipitates (Keith et al., 2021; McDermott et al., 2015; Ono et al., 2007). Our in-situ $\delta^{34}S$ data of pyrite from Brothers NW caldera shows constant values on the grain-scale, which are relatively high compared to previously published pyrite data from the same vent field (-4.7 ± 4.4 ‰, 1 s, n = 46, Martin et al., 2022b). Therefore, the combination of these two datasets suggest that a MVP-bearing fluid with low $\delta^{34}S_{H2S}$ values was diluted by isotopically heavier H_2S derived from seawater sulfate reduction, as revealed by our dataset. This dilution process is also visible in the large variation from negative to positive $\delta^{34}S_{H2S}$ (-3.2 to 7.9 ‰) values measured in vent fluids from the Brothers NW caldera (Diehl and Bach, 2020 and references therein). Due to the very low Te (~0.08 pg/g) concentration and low Te/As (4×10^{-5}) and Te/Sb (4×10^{-4}) ratios of seawater (Sohrin and Bruland, 2011), the high Te contents and high Te/As and Te/Sb ratios recorded in the pyrite rims relative to the core domains cannot be explained by fluid-seawater mixing. Seawater mixing would rather result in the dilution of the Te, As, and Sb budget and the formation of pyrite rims with low Te/As and Te/Sb ratios. In contrast to seawater, a MVP can transport substantially more Te (up to 90 µg/g) and has high Te/As (~3.0) and Te/Sb ratios (~69), as indicated by magmatic fluid inclusions (Pudack et al., 2009). Hence, high Te/As and Te/Sb values in pyrite and native S condensates, which are the result of MVP influx likely remain preserved even in hydrothermal environments that become strongly diluted by seawater-derived fluids. Since this signature is not preserved in the $\delta^{34}S$ record of pyrite from Brothers NW caldera (Fig. 6B), it is evident that the relative proportion of a MVP contribution (i.e., fluid with low $\delta^{34}S_{H2S}$) must have been minor compared to the amount of the seawater-derived fluid (i.e., fluid with relatively high $\delta^{34}S_{H2S}$ values). This suggests that the Te/As and Te/Sb ratios are more sensitive to record the contribution of a MVP than the related S isotopes systematics, if the system becomes diluted by high $\delta^{34}S_{H2S}$ fluids.

In order to verify this hypothesis, we performed mixing calculations between the H_2S portion of a seawater- and MVP-dominated

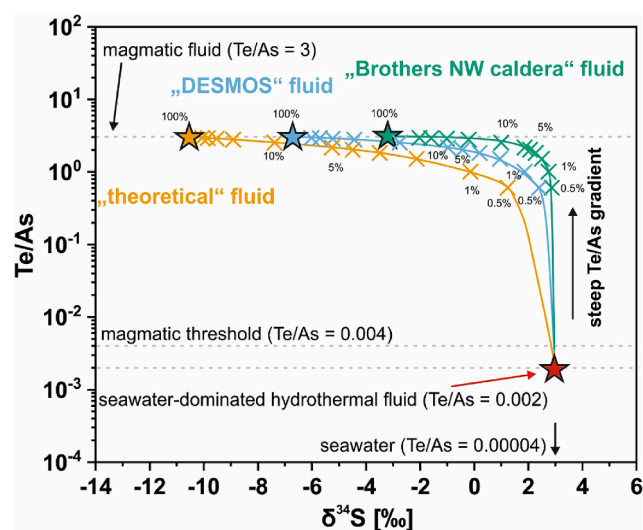**Fig. 7.** Mixing model of Te/As and $\delta^{34}S$ composition of a seawater-derived hydrothermal fluid and a magmatic volatile-dominated fluid. The crosses mark addition and mixing of 0.5, 1, 2, 3, 4, 5, 10, 20, 30, 40, and 50 % of a MVP phase to a seawater-dominated hydrothermal fluid. Mixing of small amounts of a MVP results in a steep increase in Te/As compared to only small changes in the $\delta^{34}S$ composition. This indicates that Te/As ratios are more sensitive to MVP influx than the $\delta^{34}S$ composition during influx of "low amounts" (<5 %) of a MVP into seawater-dominated fluids. Mixing modelling with Te/Sb ratios shows similar trends and are shown in the supplementary material (Fig. S7).

hydrothermal fluid (Fig. 7). As the seawater-dominated fluid endmember (i.e., no MVP fluid component), we used the fluid composition from the island arc-related Niua South vent field (Te/As = ~0.002, $\delta^{34}S_{H2S}$ = ~3 ‰, H_2S = 0.64 mmol/kg), which is the only locality where Te concentrations were reported in hydrothermal fluids lacking evidence for MVP influx (Gartman et al., 2019). We test three possible fluid compositions as potential analogues for a MVP-dominated endmember fluid, including (1) a measured vent fluid from Brothers NW caldera with the lowest $\delta^{34}S_{H2S}$ values from this site (-3.2 ‰, H_2S = 3.0 mmol/kg, Kleint et al., 2019), (2) a measured fluid from the DESMOS caldera in the Eastern Manus back-arc basin that is characterized by even lower $\delta^{34}S_{H2S}$ values (-6.7 ‰, H_2S = 8.1 mmol/kg, Gamo et al., 1997; Seewald et al., 2015), and (3) a theoretical MVP-dominated fluid. For the theoretical MVP-dominated fluid, an initial $\delta^{34}S_{SO2}$ value of 5.0 ‰ and a HSO_4^-/H_2S ratio of 3 (Eq. (1); Kusakabe et al., 2000) at 300 °C was assumed, resulting in a $\delta^{34}S_{H2S}$ value of approximately -10.5 ‰ based on the SO_2 disproportionation model from McDermott et al. (2015). For this fluid, we assume the highest measured H_2S concentration (18.5 mmol/kg, Fenway vent field, Manus basin, Seewald et al., 2015) observed in high temperature (300 °C) subduction-related MVP-dominated vent fluids, which are commonly observed in shallow (<2000 m) subduction zone-related vent fields (Diehl and Bach, 2020; Monecke et al., 2014). As an estimation of the Te and As concentration of the MVP-dominated fluid (Te/As = 3), we used the concentrations reported in an intermediate density single-phase magmatic fluid inclusion (Pudack et al., 2009), which is, to the best of our knowledge, the only quantitative Te data available for a pure magmatic fluid.

$$4SO_2 + 4H_2O \leftrightarrow H_2S + 3HSO_4^- + 3H^+ \qquad (1)$$

Our model revealed that a MVP influx of <5 % drastically changes the Te/As (and Te/Sb) ratio of a seawater-dominated fluid, but only slightly modifies its $\delta^{34}S$ composition, depending on the H_2S concentration of the respective fluids (Fig. 7 and Fig. S7). This is consistent with the results by Yang and Scott (2006), suggesting that already ~1 % of a MVP is capable of contributing up to ~85 % of the total metal budget of an ore body. Hence, mixing of a small amount of a MVP to a seawater-

dominated hydrothermal fluid can explain the steep Te/As (and Te/Sb) gradients and the comparable δ^{34}S values between the core and rim domains in pyrite from Brothers NW caldera as also revealed by trace element mapping (Fig. 6B). Consequently, the Te/As and Te/Sb values in pyrite are particularly sensitive to low degrees of MVP influx in otherwise seawater-dominated fluid, which might not be recorded by related S isotope systematics.

On this basis, we present a new discrimination diagram, which is independent of δ^{34}S constraints, using the Te/As and Te/Sb ratios in pyrite to fingerprint MVP influx in submarine subduction-related hydrothermal systems (Fig. 8). Our data demonstrate that pyrite from MVP-influenced hydrothermal systems characteristically shows elevated Te/As (>0.004) and Te/Sb (>0.6) ratios compared to pyrite that precipitated from MVP-free seawater-derived fluids. The compiled pyrite data are partly overlapping due to the large size of the dataset (n = 1378) and likely due to the varying paragenetic classification in the literature data. However, the discrimination fields agree with the Te/As and Te/Sb values of different metal reservoirs in the Earth's crust that can contribute to submarine hydrothermal systems (Fig. 8). This includes analogues for a MVP such as volcanic arc gases (Edmonds et al., 2018; Zelenski et al., 2021), single-phase intermediate density magmatic fluids from porphyry systems (Pudack et al., 2009), and native S condensates from MVP-dominated fluids from the modern seafloor (de Ronde et al., 2015; Kim et al., 2011), which consistently show Te/As (>0.004) and Te/Sb (>0.6) ratios above our newly suggested threshold for MVP-influenced submarine hydrothermal systems. By contrast and as expected, degassing-corrected arc lavas (Zelenski et al., 2021) and seawater (Sohrin and Bruland, 2011) fall within the pyrite compositional field for subduction-related hydrothermal systems that lack any evidence for a MVP contribution.

We note that our approach requires a detailed petrographic and textural evaluation of the hydrothermal pyrite in order to exclude paragenetic effects and modification of the pyrite chemistry by post-depositional hydrothermal reworking and hydrothermal system maturation, as well as high-resolution in-situ analytical techniques able to target inclusion-free as well as distinct paragenetic stages of pyrite grains. The comparison with pyrite data from mid-ocean ridge submarine hydrothermal systems revealed that the observed Te/As and Te/Sb systematics are only applicable to subduction-related settings. It remains enigmatic why some of the pyrite data from mid-ocean ridge hydrothermal systems (n = 1628) show elevated Te/As and Te/Sb values that plot into the MVP-influenced field (Fig. 8). The typically higher δ^{34}S values of sulfides from mid-ocean ridges (0 – 6 ‰; Marini et al., 2011; Seal, 2006) compared to subduction-related vent fields indicate that SO_2 disproportionation is a negligible process at mid-ocean ridge vent fields. Possible factors leading to the unexpectedly high Te/As and Te/Sb values could be the greater water depth compared to subduction-related settings, different hydrothermal fluid compositions, and/or differences in fluid-rock interaction (Hannington et al., 2005; Monecke et al., 2014; Schwarzenbach and Steele-MacInnis, 2020; Tivey, 2007), which are known to affect the chemistry of massive sulfide samples from different plate tectonic settings (e.g., Monecke et al., 2016; Toffolo et al., 2020) and might also influence the pyrite composition (Keith et al., 2016; Wohlgemuth-Ueberwasser et al., 2015). This, however, requires further investigation with a particular focus on mid-ocean ridge hydrothermal systems, which is beyond the scope of this study. In addition, the compiled literature data is difficult to sort by distinct paragenetic stages as different authors use different criteria wherefore some of the overlap and variance in the mid-ocean ridge pyrite might be related to paragenetic effects, which we however eliminated as far as possible in our data. Despite these limitations, our empirical results highlight that the Te/As and Te/Sb ratios of pyrite are a sensitive tool for fingerprinting MVP influx in submarine subduction-related hydrothermal systems – even in the presence of extensive seawater mixing, which may obscure initial MVP-related low δ^{34}S signatures.

6. Conclusions

The coupled S isotope and trace element micro-analysis of pyrite from subduction-related submarine hydrothermal systems revealed, for the first time, a direct link between δ^{34}S composition and trace element contents from the grain- to plate tectonic-scale, which we attribute to variable magmatic volatile phase contribution. On the other hand, the observed micron-scale Te/As and Te/Sb variations relative to the δ^{34}S signatures in pyrite emphasize why previous studies that were based on decoupled δ^{34}S and trace element data could not resolve such a covariation. In addition, this relation may further be obscured by paragenetic effects, as the MVP signatures are best preserved by sub- to euhedral pyrite that formed in direct contact with the endmember fluid. Therefore, our results demonstrate that isotope and trace element data in hydrothermal pyrite have a direct genetic link but require coupled high-resolution micro-analysis with detailed consideration of paragenetic and textural features.

On this basis, we developed a new discrimination diagram, which highlights that Te/As and Te/Sb ratios in pyrite are highly sensitive for fingerprinting MVP influx submarine subduction-related hydrothermal environments from the grain- to plate-tectonic-scale. Our results further demonstrate that even minor MVP contributions to otherwise seawater-dominated fluids can be traced by Te/As and Te/Sb in pyrite, while they can be concealed in the S isotope record due to the strong effect of seawater-derived S that is superimposed on the MVP signature. Mixing modelling results show that the Te/As and Te/Sb ratio in pyrite can even record a low influx <5 % of a MVP which can be temporally restricted to short term magmatic fluid pulses, as indicated by trace element mapping. Hence, Te/As and Te/Sb values in pyrite have the potential to act as a robust proxy for constraining MVP influx in subduction-related submarine hydrothermal systems.
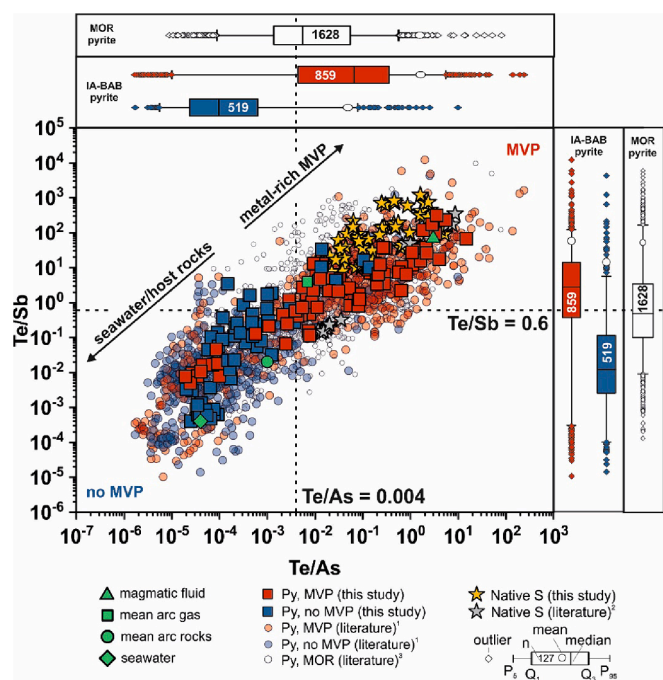

Fig. 8. Scatter Te/As – Te/Sb discrimination diagram for pyrite between MVP and no MVP subduction-related submarine hydrothermal systems. The quantitative threshold for distinguishing the two pyrite populations is defined by the average Te/As (~0.004) and Te/Sb (~0.6) ratios between the Q_3 of the MVP-free and Q_1 of the MVP-influenced pyrite group (cf. Fig. 5). Literature data from the same references as in Figs. 3 and 4. Abbreviations: MVP = magmatic volatile phase, MOR = mid-ocean ridge, IA = island arc, BAB = back-arc basin.

Data availability

Research data associated with this article can be accessed at Mendeley Data at https://doi.org/10.17632/pk3ft6wx99.1 (Falkenberg et al., 2023).

CRediT authorship contribution statement

Jan J. Falkenberg: Conceptualization, Data curation, Formal analysis, Investigation, Writing – original draft, Writing – review & editing, Visualization. **Manuel Keith:** Funding acquisition, Supervision, Writing – review & editing. **Karsten M. Haase:** Conceptualization, Funding acquisition, Supervision, Writing – review & editing. **Reiner Klemd:** Methodology, Writing – review & editing. **Martin Kutzschbach:** Formal analysis, Methodology, Writing – review & editing. **Anna Grosche:** Investigation, Methodology, Writing – review & editing. **Maria Rosa Scicchitano:** Formal analysis, Methodology, Writing – review & editing. **Harald Strauss:** Methodology, Writing – review & editing. **Jonguk Kim:** Resources.

Declaration of competing interest

The authors declare that they have no known competing financial interests or personal relationships that could have appeared to influence the work reported in this paper.

Acknowledgments

Appendix A. Supplementary material

Two supplementary files are attached to this article. The first file is a spreadsheet containing the coupled $\delta^{34}S$ SIMS and trace element LA-ICP-MS data of pyrite, additional uncoupled trace element LA-ICP-MS pyrite data, the EPMA pyrite data, the EPMA native S data, the trace element native S LA-ICP-MS data, as well as reference material data for all analytical methods. The second supplementary file consists of a more detailed description of SIMS $\delta^{34}S$ and LA-ICP-MS trace element mapping analytical procedures, additional figures, and an additional table. The additional figures contain representative time-resolved LA-ICP-MS ablation profile (Fig. S1), a compilation of new and published $\delta^{34}S$ data of hydrothermal sulfides (Fig. S2), bivariate diagrams of all trace element analyzed plotted against the coupled $\delta^{34}S$ values (Fig. S3), all LA-ICP-MS trace element maps (Fig. S4 and S5), Te/As and Te/Sb vs. $\delta^{34}S$ diagrams grouped by associated alteration assemblage from Brothers volcano (Fig. S6), and the fluid-mixing model using Te/Sb ratios and $\delta^{34}S$ (Fig. S7). The additional table (Table S1) provides information on the sample mineralogy. Supplementary material to this article can be found online at https://doi.org/10.1016/j.gca.2024.03.026.

References

Alt, J.C., et al., 1993. Cycling of sulfur in subduction zones: the geochemistry of sulfur in the Mariana Island Arc and back-arc trough. Earth Planet. Sci. Lett. 119, 477–494.

Aoyama, S., et al., 2014. Microbial sulfate reduction within the Iheya North subseafloor hydrothermal system constrained by quadruple sulfur isotopes. Earth Planet. Sci. Lett. 398, 113–126.

Auclair, G., et al., 1987. Distribution of selenium in high-temperature hydrothermal sulfide deposits at 13 degrees North, East Pacific Rise. Can. Mineral. 25, 577–587.

Belousov, I., et al., 2023. STDGL3, a reference material for analysis of sulfide minerals by laser ablation ICP-MS: an assessment of matrix effects and the impact of laser wavelengths and pulse widths. Geostand. Geoanal. Res. 47, 493–508.

Berkenbosch, H.A., et al., 2012. Mineralogy and formation of black smoker chimneys from Brothers Submarine volcano, Kermadec Arc. Econ. Geol. 107, 1613–1633.

Berkenbosch, H.A., et al., 2019. Trace element mapping of copper-and zinc-rich black smoker chimneys from Brothers volcano, kermadec arc, using synchrotron radiation XFM and LA-ICP-MS. Econ. Geol. 114, 67–92.

Börner, F., et al., 2022. In-situ trace element and S isotope systematics in pyrite from three porphyry-epithermal prospects, Limnos Island, Greece. Front. Earth Sci. 10, 1637.

Börner, F., et al., 2023. Between defects and inclusions: the fate of tellurium in pyrite. Chem. Geol. 635, 121633.

Brugger, J., et al., 2016. A review of the coordination chemistry of hydrothermal systems, or do coordination changes make ore deposits? Chem. Geol. 447, 219–253.

Butler, I.B., Nesbitt, R.W., 1999. Trace element distributions in the chalcopyrite wall of a black smoker chimney: insights from laser ablation inductively coupled plasma mass spectrometry (LA–ICP–MS). Earth Planet. Sci. Lett. 167, 335–345.

Choi, S.K., et al., 2022. Trace-element distribution and ore-forming processes in Au–Ag-rich hydrothermal chimneys and mounds in the TA25 West vent field of the Tonga arc. Miner Deposita 58, 1–26.

Choi, S.K., et al., 2023. Mineralogy and trace element geochemistry of hydrothermal sulfides from the Ari vent field, Central Indian Ridge. Miner Deposita 58, 1537–1558.

Crowe, D.E., Vaughan, R.G., 1996. Characterization and use of isotopically homogeneous standards for in situ laser microprobe analysis of 34 S/ 32 S ratios. Am. Mineral. 81, 187–193.

de Hoog, J.C., et al., 2001. Sulfur isotope systematics of basaltic lavas from Indonesia: implications for the sulfur cycle in subduction zones. Earth Planet. Sci. Lett. 189, 237–252.

de Ronde, C.E.J., et al., 2011. Submarine hydrothermal activity and gold-rich mineralization at Brothers Volcano, Kermadec arc, New Zealand. Miner Deposita 46, 541–584.

de Ronde, C.E., Chadwick, W.W., Ditchburn, R.G., Embley, R.W., Tunnicliffe, V., Baker, E.T., Walker, S.L., Ferrini, V.L., Merle, S.M. (Eds.), 2015. Molten sulfur lakes of intraoceanic arc volcanoes. Springer.

Deditius, A.P., et al., 2011. Trace metal nanoparticles in pyrite. Ore Geol. Rev. 42, 32–46.

Diehl, A., Bach, W., 2020. MARHYS (MARine HYdrothermal Solutions) database: a global compilation of marine hydrothermal vent fluid, end member, and seawater compositions. Geochem. Geophys. Geosyst. 21, e2020GC009385.

Ding, T., et al., 2001. Calibrated sulfur isotope abundance ratios of three IAEA sulfur isotope reference materials and V-CDT with a reassessment of the atomic weight of sulfur. Geochim. Cosmochim. Acta 65, 2433–2437.

Ding, T., et al., 2022. Trace-element compositions of sulfides from inactive Tianzuo hydrothermal field, Southwest Indian Ridge: implications for ultramafic rocks hosting mineralization. Ore Geol. Rev. 140, 104421.

Doebelin, N., Kleeberg, R., 2015. Profex: a graphical user interface for the Rietveld refinement program BGMN. J. Appl. Cryst. 48, 1573–1580.

Edmonds, M., et al., 2018. A distinct metal fingerprint in arc volcanic emissions. Nat. Geosci. 11, 790–794.

Edmonds, M., et al., 2022. Volcanic outgassing of volatile trace metals. Annu. Rev. Earth Planet. Sci. 50, 79–98.

Einaudi, M.T., et al., 2003. Sulfidation state of fluids in active and extinct hydrothermal systems: transitions from porphyry to epithermal environments. Special Publication-Soc. Econ. Geol. 10, 285–314.

Falkenberg, J.J., et al., 2021. Effects of fluid boiling on Au and volatile element enrichment in submarine arc-related hydrothermal systems. Geochim. Cosmochim. Acta 307, 105–132.

Falkenberg, J.J., et al., 2022. Spatial Variations in magmatic volatile influx and fluid boiling in the Submarine hydrothermal systems of Niuatahi Caldera, Tonga rear-arc. Geochem. Geophys. Geosyst. 23, e2021GC010259.

Falkenberg J., et al., 2023. Coupled in-situ SIMS d34S and LA-ICP-MS trace element data for pyrite from subduction zone related submarine hydrothermal vent fields. Mendeley Data, https://doi.org/10.17632/pk3ft6wx99.1.

Fan, L., et al., 2022. Systematic variations in trace element composition of pyrites from the 26°S hydrothermal field, Mid-Atlantic Ridge. Ore Geol. Rev. 148, 105006.

Fouquet Y., et al., 1993. Metallogenesis in back-arc environments: The Lau basin example. *Economic Geology (plus the Bulletin of the Society of Economic Geologists); (United States)* 88:8.

Früh-Green, G.L., et al., 2022. Diversity of magmatism, hydrothermal processes and microbial interactions at mid-ocean ridges. Nat. Rev. Earth Environ. 3, 1–20.

AG Galley, Koski R. A. (1999) Setting and characteristics of ophiolite-hosted volcanogenic massive sulfide deposits. In: Barrie, C.T., Hannington, M.D. (Eds.) Volcanic-associated massive sulfide deposits: processes and examples in modern and ancient settings. Rev. Econ. Geol 8, 221–246.

Gamo, T., et al., 1997. Acidic and sulfate-rich hydrothermal fluids from the Manus back-arc basin, Papua New Guinea. Geol 25, 139–142.

Gartman, A., et al., 2019. The role of nanoparticles in mediating element deposition and transport at hydrothermal vents. Geochim. Cosmochim. Acta 261, 113–131.

GEBCO Bathymetric Compilation Group, 2020 *The GEBCO_2020 Grid - a continuous terrain model of the global oceans and land.* British Oceanographic Data Centre, National Oceanography Centre, NERC, UK.

González-Jiménez, J.M., et al., 2022. Polymetallic nanoparticles in pyrite from massive and stockwork ores of VMS deposits of the Iberian Pyrite Belt. Ore Geol. Rev. 145, 104875.

González-Partida, E., et al., 2005. Hydro-geochemical and isotopic fluid evolution of the Los Azufres geothermal field, Central Mexico. Appl. Geochem. 20, 23–39.

Grant, H.L., et al., 2018. Constraints on the behavior of trace elements in the actively-forming TAG deposit, Mid-Atlantic Ridge, based on LA-ICP-MS analyses of pyrite. Chem. Geol. 498, 45–71.

Grosche, A., et al., 2023. Sources, transport, and deposition of metal(loid)s recorded by sulfide and rock geochemistry: constraints from a vertical profile through the epithermal Profitis Ilias Au prospect, Milos Island, Greece. Miner Deposita 58, 1101–1122.

Grosche, A., et al., 2024. Temperature-controlled Se-S isotope fractionation during seawater mixing and sulfide precipitation in black smoker chimneys. Geochim. Cosmochim. Acta 372, 13–27.

Grundler, P.V., et al., 2013. Speciation of aqueous tellurium (IV) in hydrothermal solutions and vapors, and the role of oxidized tellurium species in Te transport and gold deposition. Geochim. Cosmochim. Acta 120, 298–325.

Habicht, K.S., Canfield, D.E., 1997. Sulfur isotope fractionation during bacterial sulfate reduction in organic-rich sediments. Geochim. Cosmochim. Acta 61, 5351–5361.

Hannington, M.D., et al., 2005. Sea-floor tectonics and submarine hydrothermal systems. Econ. Geol. 100, 111–141.

Herzig, P.M., et al., 1998. Sulfur isotopic composition of hydrothermal precipitates from the Lau back-arc: implications for magmatic contributions to seafloor hydrothermal systems. Miner. Deposita 33, 226–237.

Huston, D.L., et al., 1995. Trace elements in sulfide minerals from eastern Australian volcanic-hosted massive sulfide deposits; Part I, Proton microprobe analyses of pyrite, chalcopyrite, and sphalerite, and Part II, Selenium levels in pyrite; comparison with delta 34 S values and implications for the source of sulfur in volcanogenic hydrothermal systems. Econ. Geol. 90, 1167–1196.

Keith, M., et al., 2016. Trace element systematics of pyrite from submarine hydrothermal vents. Ore Geol. Rev. 72, 728–745.

Keith, M., et al., 2018. A review of Te and Se systematics in hydrothermal pyrite from precious metal deposits: insights into ore-forming processes. Ore Geol. Rev. 96, 269–282.

Keith, M., et al., 2021. Trace element fractionation and precipitation in submarine back-arc hydrothermal systems, Nifonea caldera, New Hebrides subduction zone. Ore Geol. Rev. 135, 104211.

Kim, J., et al., 2011. Metal-bearing molten sulfur collected from a submarine volcano: implications for vapor transport of metals in seafloor hydrothermal systems. Geol 39, 351–354.

Kleint, C., et al., 2019. Geochemical characterization of highly diverse hydrothermal fluids from volcanic vent systems of the Kermadec intraoceanic arc. Chem. Geol. 528, 119289.

Klose, L., et al., 2021. Trace element and isotope systematics in vent fluids and sulphides from Maka volcano, North Eastern Lau spreading centre: insights into three-component fluid mixing. Front. Earth Sci. 9.

Klose, L., et al., 2022. Hydrothermal activity and associated subsurface processes at Niuatahi rear-arc volcano, North East Lau Basin, SW Pacific: implications from trace elements and stable isotope systematics in vent fluids. Geochim. Cosmochim. Acta 332, 103–123.

Koschinsky, A., et al., 2008. Hydrothermal venting at pressure-temperature conditions above the critical point of seawater, 5°S on the Mid-Atlantic Ridge. Geol 36, 615.

Kusakabe, M., et al., 2000. Sulfur isotopic effects in the disproportionation reaction of sulfur dioxide in hydrothermal fluids: implications for the $\delta^{34}S$ variations of dissolved bisulfate and elemental sulfur from active crater lakes. J. Volcanol. Geoth. Res. 97, 287–307.

Layton-Matthews, D., et al., 2013. Multiple sources of selenium in ancient seafloor hydrothermal systems: compositional and Se, S, and Pb isotopic evidence from volcanic-hosted and volcanic-sediment-hosted massive sulfide deposits of the Finlayson Lake District, Yukon, Canada. Geochim. Cosmochim. Acta 117, 313–331.

Liao, S., et al., 2021. Distal axis sulfide mineralization on the ultraslow-spreading Southwest Indian Ridge: an LA-ICP-MS study of pyrite from the East Longjing-2 hydrothermal field. Acta Oceanol. Sin. 40, 105–113.

Lüders, V., et al., 2001. Fluid inclusion and sulfur isotope studies in probable modern analogue Kuroko-type ores from the JADE hydrothermal field (Central Okinawa Trough, Japan). Chem. Geol. 173, 45–58.

Lupton, J., et al., 2015. Helium isotope, C/3He, and Ba-Nb-Ti signatures in the northern Lau Basin: distinguishing arc, back-arc, and hotspot affinities. Geochem. Geophys. Geosyst. 16, 1133–1155.

Mandon, C.L., et al., 2020. Volatile transport of metals and the Cu budget of the active White Island magmatic-hydrothermal system, New Zealand. J. Volcanol. Geoth. Res. 398, 106905.

Marini, L., et al., 2011. Sulfur isotopes in magmatic-hydrothermal systems, melts, and magmas. Rev. Mineral. Geochem. 73, 423–492.

Martin, A.J., et al., 2020. Effects of magmatic volatile influx in mafic VMS hydrothermal systems: evidence from the Troodos ophiolite, Cyprus. Chem. Geol. 531, 119325.

Martin, A.J., et al., 2022a. Mineral-scale variation in the trace metal and sulfur isotope composition of pyrite: implications for metal and sulfur sources in mafic VMS deposits. Miner. Deposita 57, 911–933.

Martin, A.J., et al., 2022b. Trace metal and sulfur cycling in a hydrothermally active arc volcano: deep-sea drilling of the Brothers volcano, Kermadec arc, New Zealand. Miner. Deposita 58, 430.

Martin, A.J., et al., 2023a. Constraining temporal variations in metal and sulfur sources using high-resolution mineral-scale analysis of pyrite: evidence from the Brothers volcano, Kermadec arc, New Zealand. Miner. Deposita 58, 1237–1262.

Martin, A.J., et al., 2023b. Hydrothermal alteration within the Brothers submarine arc volcano, Kermadec arc, New Zealand. Econ. Geol. 118 (7), 1657–1679.

Maslennikov, V.V., et al., 2009. Study of trace element zonation in vent chimneys from the Silurian Yaman-Kasy volcanic-hosted massive sulfide deposit (Southern Urals, Russia) using laser ablation-inductively coupled plasma mass spectrometry (LA-ICPMS). Econ. Geol. 104, 1111–1141.

Maslennikov, V.V., et al., 2020. Pyrite Varieties at Pobeda hydrothermal fields, Mid-Atlantic Ridge 17° 07′–17° 08′ N: LA-ICP-MS data deciphering. Minerals 10, 622.

McDermott, J.M., et al., 2015. Identification of sulfur sources and isotopic equilibria in submarine hot-springs using multiple sulfur isotopes. Geochim. Cosmochim. Acta 160, 169–187.

McKibben, M.A., Eldridge, C.S., 1990. Radical sulfur isotope zonation of pyrite accompanying boiling and epithermal gold deposition; a SHRIMP study of the Valles Caldera, New Mexico. Econ. Geol. 85, 1917–1925.

Melekestseva, I., et al., 2018. Sulfide breccias from the Semenov-3 hydrothermal field, Mid-Atlantic Ridge: authigenic mineral formation and trace element pattern. Minerals 8, 321.

Melekestseva, I., et al., 2020. Trace element geochemistry of sulfides from the Ashadze-2 hydrothermal field (12°58′ N, Mid-Atlantic Ridge): influence of host rocks, formation conditions or seawater? Minerals 10, 743.

Meng, X., et al., 2019. Multi-stage growth and fluid evolution of a hydrothermal sulphide chimney in the East Pacific Ridge 1–2° S hydrothermal field: constraints from in situ sulphur isotopes. Geol. Mag. 156, 989–1002.

Meng, X., et al., 2020. Trace element and sulfur isotope compositions for pyrite across the mineralization zones of a sulfide chimney from the East Pacific rise (1–2°S). Ore Geol. Rev. 116, 103209.

Metz, S., Trefry, J.H., 2000. Chemical and mineralogical influences on concentrations of trace metals in hydrothermal fluids. Geochim. Cosmochim. Acta 64, 2267–2279.

Monecke, T., et al., 2014. Constraints on water depth of massive sulfide formation: evidence from modern seafloor hydrothermal systems in arc-related settings. Econ. Geol. 109, 2079–2101.

Monecke, T., et al., 2016. The minor element endowment of modern sea-floor massive sulfide deposits and comparison with deposits hosted in ancient volcanic successions. Rev. Econ. Geol. 18, 245–306.

Nozaki, T., et al., 2021. Microbial sulfate reduction plays an important role at the initial stage of subseafloor sulfide mineralization. Geol 49, 222–227.

Ono, S., et al., 2007. S-33 constraints on the seawater sulfate contribution in modern seafloor hydrothermal vent sulfides. Geochim. Cosmochim. Acta 71, 1170–1182.

Palarea-Albaladejo, J., Martín-Fernández, J.A., 2013. Values below detection limit in compositional chemical data. Anal. Chim. Acta 764, 32–43.

Paton, C., et al., 2011. Iolite: freeware for the visualisation and processing of mass spectrometric data. J. Anal. At. Spectrom. 26, 2508.

Peters, C., et al., 2021. SO2 disproportionation impacting hydrothermal sulfur cycling: insights from multiple sulfur isotopes for hydrothermal fluids from the Tonga-Kermadec intraoceanic arc and the NE Lau Basin. Chem. Geol. 586, 120586.

Petersen, S., et al., 2018. Modern seafloor hydrothermal systems: new perspectives on ancient ore-forming processes. Elements: An Int. Mag. Mineral. Geochem. Petrol. 14, 307–312.

Pokrovski, G.S., et al., 2013. Speciation and transport of metals and metalloids in geological vapors. Rev. Mineral. Geochem. 76, 165–218.

Pudack, C., et al., 2009. Evolution of magmatic vapor to gold-rich epithermal liquid: the porphyry to epithermal transition at Nevados de Famatina, northwest Argentina. Econ. Geol. 104, 449–477.

Reed, M.H., Palandri, J., 2006. Sulfide mineral precipitation from hydrothermal fluids. Rev. Mineral. Geochem. 61, 609–631.

Reeves, E.P., et al., 2011. Geochemistry of hydrothermal fluids from the PACMANUS, Northeast Pual and Vienna Woods hydrothermal fields, Manus basin, Papua New Guinea. Geochim. Cosmochim. Acta 75, 1088–1123.

Reich, M., et al., 2005. Solubility of gold in arsenian pyrite. Geochim. Cosmochim. Acta 69, 2781–2796.

Román, N., et al., 2019. Geochemical and micro-textural fingerprints of boiling in pyrite. Geochim. Cosmochim. Acta 246, 60–85.

Sahlström, F., et al., 2023. Mineralogical distribution and genetic aspects of cobalt at the active Fåvne and Loki's Castle seafloor massive sulfide deposits, Arctic mid-Ocean Ridges. Ore Geol. Rev. 153, 105261.

Schaarschmidt, A., et al., 2021. Boiling effects on trace element and sulfur isotope compositions of sulfides in shallow-marine hydrothermal systems: evidence from Milos Island, Greece. Chem. Geol. 583, 120457.

Schmidt, K., et al., 2017. Boiling vapour-type fluids from the nifonea vent field (new hebrides back-arc, vanuatu, sw pacific): geochemistry of an early-stage, post-eruptive hydrothermal system. Geochim. Cosmochim. Acta 207, 185–209.

Schwarzenbach, E.M., Steele-MacInnis, M., 2020. Fluids in Submarine Mid-Ocean ridge hydrothermal settings. Elements 16, 389–394.

Seal, R.R., 2006. Sulfur isotope geochemistry of sulfide minerals. Rev. Mineral. Geochem. 61, 633–677.

Seewald, J.S., et al., 2015. Submarine venting of magmatic volatiles in the Eastern Manus Basin, Papua New Guinea. Geochim. Cosmochim. Acta 163, 178–199.

Sohrin, Y., Bruland, K.W., 2011. Global status of trace elements in the ocean. TrAC Trends Anal. Chem. 30, 1291–1307.

Stoffers, P., et al., 2006. Submarine volcanoes and high-temperature hydrothermal venting on the Tonga arc, southwest Pacific. Earth Planet. Sci. Lett. 34, 453.

Stucker, V.K., et al., 2022. Rare time series of hydrothermal fluids for a submarine volcano: 14 years of vent fluid compositions for Brothers Volcano, Kermadec Arc New Zealand. Econ. Geol. 118, 1536–1576.

Sylvester, P.J., 2001. Laser-ablation-ICPMS in the earth sciences: principles and applications. Mineralogical association of Canada Short Course Series 40:356 pp.

Tivey, M.K., 2007. Generation of seafloor hydrothermal vent fluids and associated mineral deposits. Oceanography 20, 50–65.

Toffolo, L., et al., 2020. Seafloor massive sulfides from mid-ocean ridges: exploring the causes of their geochemical variability with multivariate analysis. Earth Sci. Rev. 201, 102958.

Tostevin, R., et al., 2014. Multiple sulfur isotope constraints on the modern sulfur cycle. Earth Planet. Sci. Lett. 396, 14–21.

Ueda, A., Sakai, H., 1984. Sulfur isotope study of Quaternary volcanic rocks from the Japanese Islands Arc. Geochim. Cosmochim. Acta 48, 1837–1848.

Wang, S., et al., 2017a. Mineralogical characteristics of polymetallic sulfides from the Deyin-1 hydrothermal field near 15 S, southern Mid-Atlantic Ridge. Acta Oceanol. Sin. 36, 22.

Wang, Y., et al., 2017b. Mineralogy and trace element geochemistry of sulfide minerals from the Wocan Hydrothermal Field on the slow-spreading Carlsberg Ridge, Indian Ocean. Ore Geol. Rev. 84, 1–19.

Wang, Y., et al., 2018. Trace metal distribution in sulfide minerals from ultramafic-hosted hydrothermal systems: examples from the Kairei Vent Field, Central Indian Ridge. Minerals 8, 526.

Wang, H., et al., 2020. Mineralogy, geochemistry, and Sr–Pb and in situ S isotopic compositions of hydrothermal precipitates from the Tangyin hydrothermal field, southern Okinawa Trough: evaluation of the contribution of magmatic fluids and sediments to hydrothermal systems. Ore Geol. Rev. 126, 103742.

Wang, S., et al., 2022. Constraints on fluid evolution and growth processes of black smoker chimneys by pyrite geochemistry: a case study of the Tongguan hydrothermal field, South mid-Atlantic Ridge. Ore Geol. Rev. 140, 104410.

Wilson, S.A., et al., 2002. Development of sulfide calibration standards for the laser ablation inductively-coupled plasma mass spectrometry technique. J. Anal. At. Spectrom. 17, 406–409.

Wohlgemuth-Ueberwasser, C.C., et al., 2015. Distribution and solubility limits of trace elements in hydrothermal black smoker sulfides: an in-situ LA-ICP-MS study. Geochim. Cosmochim. Acta 159, 16–41.

Woodhead, J.D., et al., 1987. O, S, Sr, and Pb isotope variations in volcanic rocks from the Northern Mariana Islands: implications for crustal recycling in intra-oceanic arcs. Earth Planet. Sci. Lett. 83, 39–52.

Yang, K., Scott, S.D., 2006. Magmatic fluids as a source of metals in seafloor hydrothermal systems. Washington DC Am. Geophys. Union Geophys. Monogr. Ser. 166, 163–184.

Yuan, B., et al., 2018. Geochemistry of pyrite and chalcopyrite from an active black smoker in 49.6° E Southwest Indian Ridge. Mar. Geophys. Res. 39, 441–461.

Zelenski, M., et al., 2021. Partitioning of elements between high-temperature, low-density aqueous fluid and silicate melt as derived from volcanic gas geochemistry. Geochim. Cosmochim. Acta 295, 112–134.

Zhang, Y., et al., 2020. Gold enrichment in hydrothermal sulfides from the Okinawa Trough: an in situ LA-ICP-MS study. Ore Geol. Rev. 116, 103255.

Zhang, H., et al., 2023. Occurrence and precipitation mechanism of silver in pyrite from chimney fragments in the Edmond hydrothermal field, Central Indian Ridge. Ore Geol. Rev. 158, 105471.